Cite as: Meng J, Dai K,Zhao Z,Mao Z, Camara A, Zhang S and Mei Z (2020). Study on the aerodynamic damping for the seismic analysis of wind turbines in operation. Renewable Energy (in press). DOI: 10.1016/j.renene.2020.05.181.

Study on the aerodynamic damping for the seismic analysis of wind turbines in operation

Abstract

The continuous cost reduction of wind turbines has consolidated the competitiveness of wind energy. With the increasing installation of wind turbines in seismic-prone regions, it is likely that earthquakes will strike farms in operation. A practical approach to predict the dynamic behavior of a wind turbine under simultaneous seismic and operational wind loads is investigated in this work. The combined action can be determined by analyzing the wind and the seismic-induced responses separately. However, an accurate definition of the aerodynamic damping is required for this purpose and there are few experimental studies on the additional damping source. A 1/100-scaled wind turbine model was designed and the aerodynamic damping of the model was identified. Subsequently, the ground motion was applied in the model by means of a shake table and the combined wind/earthquake response that was measured experimentally was compared with the response predicted by several combination rules. A numerical study using the FAST analysis package for wind turbines was also conducted to complement the experiments with fully-coupled simulations that include aeroelastic effects. This work provides a necessary experimental reference for structural engineers to use adequate aerodynamic damping and load combination methods for the seismic analysis of wind turbines in operation.

Keywords

Wind turbine model; Experimental study; Aerodynamic damping; Wind-seismic interaction.

1. Introduction

Wind energy has gained soaring momentum worldwide and it became one of the most competitive sources of renewable energy. Overall, the year of 2018 has witnessed a global wind power installation of 51.3 GW, bringing the total capacity as 591 GW [1]. According to the latest report of the International Renewable Energy Agency (IRENA) [2], the global weighted average cost of electricity from onshore wind has declined by 34% since 2010, to around 0.056 USD/kWh, which has demonstrated itself as one of the most promising sources of energy to replace the traditional fossil fuel.

One of the crucial aspects in wind turbine design is to provide reliable supporting structures, which generally involves the determination of the effects of aerodynamic, inertial and operational loads, as well as the soil-structure interaction [3, 4]. Moreover, with the increasing number of wind turbines installed in seismic-prone regions, for example, in the Pacific Rim and in the Mediterranean Sea areas [5], the seismic actions are potentially dominant in the dynamic responses of these structures [6, 7]. In recent years a number of authors have studied the seismic behavior of wind turbines [5, 8 – 11]. The aerodynamic loads were not considered in these works because it was assumed that an emergency shutdown would be triggered if the acceleration of the nacelle reaches the safety threshold [12]. However, it is likely that strong ground motions would strike operating wind turbines before the blades are fully feathered and stop rotating, adding potentially unfavorable loads that may govern the tower design [13]. In light of this, the seismic analysis of wind turbines under operational conditions has attracted increasing interest, the emphasis of which is on the interaction between the aerodynamic and the earthquake actions [14 – 17]. Earthquake-induced oscillations of the turbine affect the aerodynamic loads and vice versa [18]. Hence, full aeroelastic analysis including the inherent interaction is recommended [4]. Software packages that are specific for wind turbines such as FAST [19] and GH Bladed [20] can be used to predict the seismic performance combined with the aerodynamic loading. These numerical tools can be accurate but they require a significant computational effort because of the need for repetitive simulations to be performed for all the selected earthquake records and the different wind environment scenarios [18, 21]. On account of

this, some international standards and design guidelines propose simplified uncoupled analyses in which the aerodynamic and the seismic responses are calculated separately and then combined [13, 22, 23].

The interaction between the vibrating blades and the wind field can be considered in a quasi-steady approach by means of the adequate definition of the aerodynamic damping in the seismic analysis [24]. The modification of the relative wind velocity at the blades induced by the blade vibration during the earthquake changes the local angle of attack and thus it affects the aerodynamic force. Before the blades enter a stall condition, the increment of the aerodynamic force is always opposite to the direction of the tower motion, which provides an effect equivalent to a viscous damper that mitigates the vibration of the tower [25]. The determination of this additional damping effect is necessary to obtain accurate design loads as well as to help proposing vibration control schemes [26]. Dai et al. [27] conducted a field measurement of a 1.5-MW horizontal-axis wind turbine (HAWT). When the blades started rotating for rated-power generation, an increase in the damping ratio of the fundamental vibration mode of the tower (from 1.8% to 3.2%) was observed, which is due to the aerodynamic damping effect. Dong et al. [28] launched a long-term prototype observation of a 2.5-MW offshore HAWT. The overall damping ratio measured in this work ranges from 1.07% to 9.98% under different operational conditions. The overall damping includes the inherent dissipation from the structure and the soil, as well as the aerodynamic and the hydrodynamic (when applicable) damping effects [29]. The aerodynamic damping can be much higher than the other sources of dissipation, especially for large-scale wind turbines. Liu et al. [25] carried out a load analysis on a 5-MW offshore HAWT, and reported a great reduction of the average vibration amplitudes of the tower (from 1.94 m to 0.22 m) when the aerodynamic damping effect is included. Therefore, the inappropriate consideration of aerodynamic damping may change the response prediction significantly, leading to either unreliable or to over-conservative designs.

Increasing efforts have been made to quantify the aerodynamic damping effect in numerical analyses of the seismic response. Witcher [30] examined combined wind and earthquake loading in a 2-MW HAWT using the GH Bladed software. He noticed that the peak tower response obtained in the fully-coupled time-domain analysis could be approximated by the response-spectrum approach with 5% damping ratio. This is convenient because the damping ratio reference in the seismic design spectra for buildings in ASCE/SEI 7-10 [31] is set to 5%. ASCE/AWEA [13] recommends that the overall damping ratio should be set to 1% for parked conditions and to 5% for operational conditions (i.e. 1% structural damping ratio plus 4% aerodynamic damping ratio). Valamanesh and Myers [32] complemented the damping values provided by ASCE/AWEA [13] from numerical simulations conducted using FAST for the dynamic analysis of a 1.5-MW HAWT. They recommended 5% damping ratio for operational conditions in the fore-aft direction, while 1% is used for parked conditions in both directions and for operational conditions in the side-side direction. Avossa et al. [24] investigated a decoupled model for the vulnerability assessment of a 5-MW HAWT subjected to wind and seismic actions, within which the aerodynamic damping was predicted from the proposal of Valamanesh and Myers [32], namely 0.1% for the parked condition, 3.7% in the fore-aft direction and 1% in the side-side direction for the operational condition. However, the experimental studies on this topic are rather scarce. The exception is the shake table test on an actual 65-kW HAWT conducted at the University of California, San Diego [33]. This work concluded that the aerodynamic damping has an appreciable effect in the fore-aft response, while it may be negligible in the side-side direction.

Several theoretical models of the aerodynamic damping are summarized in Table 1, from which it can be concluded that the aerodynamic damping mainly depends on the rotor speed, the derivative of the lift coefficient with respect to the angle of attack (C_L') and the blade geometry. Garrad [34] derived a simplified analytical expression of the aerodynamic damping on a blade element of unit length, which was subsequently rewritten by Kühn [35] to obtain the aerodynamic damping for the entire rotor. Salzmann and Van der Tempel [36] modified Kühn's model by including a correction factor to allow it to be applied on modern variable-speed wind turbines. These studies assumed small inflow angles and high tip speed ratios for the operating wind turbine, and therefore they ignored the contributions from the wind speed and from the aerodynamic drag, which may underestimate the aerodynamic damping at high wind speeds.

In addition, they are only able to estimate the fore-aft aerodynamic damping. Valamanesh and Myers [32] extended on these studies by including the wind speed and the drag terms, as well as by providing a method to estimate the aerodynamic damping in the side-side direction. However, important assumptions such as considering steady, uniform wind conditions are made, and consequently the applicability of the method needs to be validated experimentally.

Table 1. Summary of techniques to estimate the aerodynamic damping coefficient (the nomenclature can be found in the Appendix).

Researchers	Assumptions	Techniques
Garrad [34]	• rigid rotor • constant rotor speed • small inflow angle • high tip speed ratio • attached flow	$c_{fore-aft}=\frac{\rho\Omega rc}{2}C_L'$ (for a blade element of unit length)
Kühn [35]	• rigid rotor • constant rotor speed • small inflow angle • high tip speed ratio • attached flow	• closed-form linearization: $c_{fore-aft}=\frac{N_b\rho\Omega}{2}\int_{R_{hub}}^{R}C_L'\big\vert_r c(r)r\mathrm{d}r$ • numerical linearization • non-linear time-domain simulation
Salzmann and Van der Tempel [36]	• rigid rotor • variable rotor speed • small inflow angle • high tip speed ratio • attached flow	• closed-form solution: $c_{fore-aft}=\frac{N_b\rho\Omega(V_W)}{2}\int_{R_{hub}}^{R}C_L'\big\vert_r bc(r)r\mathrm{d}r$ • simulation method: $c_{fore-aft}=\frac{\mathrm{d}T}{\mathrm{d}V_W}$
Valamanesh and Myers [34]	• rigid rotor • three-bladed rotor • steady, uniform wind • wind perpendicular to the rotor plane	$c_{fore-aft}=N_b\int_{R_{hub}}^{R}\left\{\rho V_W(1-a)(C_L\cos\varphi+C_D\sin\varphi)+\frac{\rho}{2}\Omega r(1+a')[(C_L'+C_D)\cos\varphi+(C_D'-C_L)\sin\varphi]\right\}c(r)\mathrm{d}r$ $c_{side-side}=\frac{N_b}{2}\int_{R_{hub}}^{R}\left\{\rho\Omega r(1+a')(C_L\sin\varphi-C_D\cos\varphi)-\frac{\rho}{2}V_W(1-a)[(C_L'+C_D)\sin\varphi+(C_L-C_D')\cos\varphi]\right\}c(r)\mathrm{d}$

With the aerodynamic damping, the seismic demand can be determined either in response-spectrum analysis or in time-domain analysis [21]. In practice, the peak responses (e.g. the peak tower base moment or the peak shear force) due to the operational wind actions and due to the ground motions can be calculated separately and then combined considering that the corresponding peak responses may not occur at the same time. ASCE/AWEA [13] recommends to calculate the earthquake and the aerodynamic demands independently and then multiply the sum of the two demands by a reduction factor of 0.75. The recommendation also argues that the combination factor of 1 (which means adding directly the two demands) that is proposed in IEC 61400-1 [22] and GL [23] may overestimate the dynamic response. Asareh et al. [16] and Santangelo et al. [21] studied a 5-MW HAWT individually, and showed that the combination of seismic and aerodynamic loads with load factor of 0.75 can provide results that are sufficiently close to the fully-coupled simulations. Prowell [14] combined separate seismic and wind analyses for 65-kW, 900-kW, 1.5-MW, and 5-MW wind turbines. The results were compared with the fully-coupled FAST simulations. It was observed that combining the two separate responses with the square root of the sum of the squares (SRSS) gives better results than simply adding the response maxima directly, especially for large-scale wind turbines. Yang et al. [37] investigated the dynamic behavior of a 5-MW HAWT under various earthquake intensities and concluded that the load combinations presented by ASCE/AWEA [13] and by Prowell [14] tend to provide more accurate results than the direct combination method.

To sum up, two main tasks are involved in the simplified seismic analysis of wind turbines in operation. One is to choose an appropriate aerodynamic damping for the assessment of separate earthquake responses, and the other is to adopt a reliable method to combine the separate earthquake and wind responses. These two subjects have been mainly investigated numerically in previous research works. However, considering the highly unstable flow conditions that the wind turbines experience in real situations, the applicability of the proposed damping ratios and combination rules requires further experimental verification, on which few published works are available. In light of the difficulties of

building a full-scale model test of a wind turbine because of space limitations and complex control systems installed in the nacelle, the present paper designed a simplified 1/100-scaled wind turbine model. The aerodynamic damping coefficients identified experimentally were compared to those calculated by different methods proposed in the literature to recommend a practical approach that determines the level of aerodynamic damping effect. Afterwards, different combination rules were investigated experimentally on the wind turbine model by means of shake table tests to obtain a better prediction of the wind-seismic responses. Numerical simulation in FAST was also conducted to explore the load combination rules under different ratios of the wind/seismic response and the validity of the fan-generated wind field in the experiments, as well as the effect of higher order tower modes and the side-side ground shaking in the response (which was not applied in the experiments).

2. Wind turbine model design and experimental setup

The laboratory model is scaled based on the Nordex S70/1.5 MW wind turbine with a rotor diameter of 70 m and a hub height of 64.65 m. The scheme of the similarity criteria is shown in Table 2, in which the scaling factors of length, Young's modulus and acceleration are set to control the geometrical scale, material and shake table testing, respectively. It is known that the aerodynamic performance of the rotor depends largely on the behavior of the wind flow around the blade section and, in turn, on the Reynolds number (*Re*). Compared with the full-scale 1.5-MW wind turbine rotor which yields a *Re* of around 3.9×10^6 when operating at a rotor speed of 20 rpm under a wind speed of 13 m/s, the *Re* of the geometrically-scaled rotor can be reduced to 5500. This corresponds to a very low *Re* regime that potentially presents significant laminar flow separation and the reduction of the aerodynamic performance of the airfoil at the model scale [38].

Table 2. Scheme of the scaling factors (λ) for the wind turbine model testing

Parameter	Units	Scale	Scale Value
Length	L	λ_L	0.01
Young's modulus	$ML^{-1}T^{-2}$	λ_E	0.3495
Acceleration	LT^{-2}	λ_a	2
Time	T	$\lambda_L{}^{0.5}\lambda_a{}^{-0.5}$	0.0707

As it is summarized in Table 3, the *Re* scaling issue has been discussed in detail over the past few years for the wind turbine model design in a wide range of geometric scaling factors from 1/440 to 1/35. The mismatch of the *Re* and, therefore, of the aerodynamic behavior of the model turbine could be generally compensated with three methods: 1) increasing the model wind speed to increase the *Re* directly; 2) redesigning the blade by using specific low-*Re* airfoils; 3) using turbulators (like dots or strips on the leading edge of the blade surface) to facilitate the transition from laminar to turbulent flow around the blade at low *Re*, delaying the separation and hence improving the aerodynamic efficiency of the model [39]. Compared with the first approach, which may not capture the aerodynamic damping effects correctly and the third one which could result in an erratic rotor behavior, the second method is the most common one in previous studies [40]. This is the approach adopted in this work, in which the goal is not to extrapolate the behavior of the scaled model to that of a particular full-scale wind turbine, but to provide experimental support to the estimation of the aerodynamic damping of wind turbines subject to ground motions by means of the operational data and structural vibrations that were recorded in this research from a turbine model under relatively controlled operating conditions. For this reason, the similitude ratios in the design of the blades and in the wind and the rotational speeds were not considered, redesigning the blades to obtain relevant aerodynamic damping effects in the scaled model of the turbine during the experiments. One of the typical low-*Re* airfoils, the Eppler 387 (E387), was chosen because it has been thoroughly studied and there is a wealth of experimental data available that covers a wide range of *Re* from 10,000 to 500,000 [41 – 44]. McArthur [44] reported reliable experimental results of

149 the E387 airfoil characteristics at low Reynolds numbers (from 10,000 to 60,000). His results are therefore applied
150 in the aerodynamic damping study in this paper.

151 Table 3. Summary of scaling design for wind turbines in previous research works.

Literature	Prototype	Scale	Model *Re* ($\times 10^4$)	Increase wind speed	Redesign bade	Use turbulators
Hassanzadeh et al. [45]	NREL 1.5 MW	1/35	10 – 35		√	√
Ryi et al. [46]	750 kW	1/36	≈ 23			√
Battasso et al. [47]	Vestas 3 MW	1/45	5 – 6		√	√
Martin [40]	NREL 5 MW	1/50	≈ 3.57	√		√
Li et al. [48]	NREL 5 MW	1/50	≈ 3.25	√		
Duan et al. [49]	NREL 5 MW	1/50	4.44 – 8.88		√	
Berger et al. [50]	NREL 5 MW	1/70	5 – 14		√	
Bayati et al. [51]	DTU 10 MW	1/75	3 – 25		√	
Nano et al. [52]	DTU 10 MW	1/200	3 – 5		√	
Coudou et al. [53]	Vestas 2 MW	1/440	≈ 3.5		√	

152 The mathematical model for the blade design is based on the Blade Element Momentum (BEM) theory. The design
153 is initialized by setting the airfoil characteristics at the corresponding value of *Re* and introducing the parameters of the
154 wind turbine under consideration from Table 4. The rotational axis of the blade (i.e. the aerodynamic center of the airfoil)
155 is fixed at 1/4 chord. A nonlinear constrained optimization follows to improve the efficiency by maximizing the local
156 power coefficient (C_p) at each annular blade element. The Prandtl's tip/root loss factor is also introduced in the design
157 algorithm to correct the assumption of infinite number of blades in the BEM theory [4]. The design methodology
158 presented in Ref. [3, 54, 55] are comprehensively considered and the process is illustrated in Fig. 1.

159 Table 4. Specifications of the wind turbine model.

Parameter	Value	Parameter	Value
Number of blades	3	Rotor radius R (mm)	240
Rated power (W)	16	Hub radius R_{hub} (mm)	40
Rated wind speed (m/s)	7	Tower height (mm)	630
Rated rotor speed (rpm)	1000	Mass of blades (kg)	0.300
Initial tip speed ratio	3.4	Tower mass (kg)	0.206
Initial power coefficient	0.41	Total tower-top mass (kg)	1.169

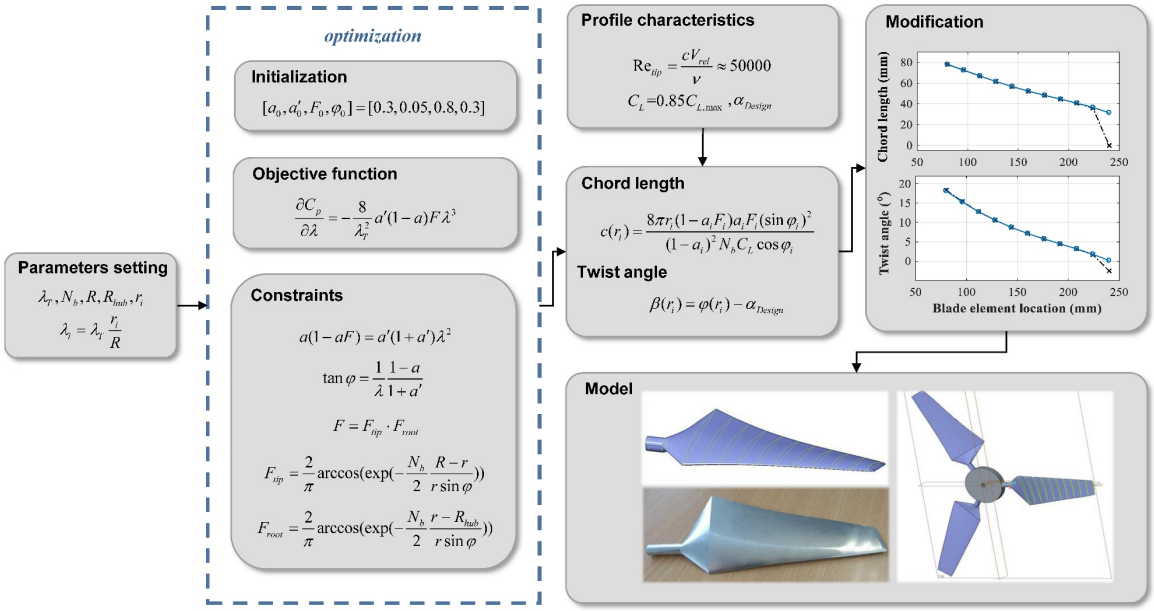

Fig. 1. Blade design procedure (the nomenclature can be found in the Appendix).

After modifying the chord length and the twist angle distribution, the blades were manufactured from aluminum alloy by means of digital carving. The supporting system of the three-bladed rotor contains a ball bearing, an aluminum tube and a bottom base (Fig. 2). Bolted connections were used between the tube and the base, between the tube and the top mass, and between the blades and the rotor hub to facilitate the assembly and disassembly of the model. A manually adjusted pitch device was also set at the root of the blades. This allows the rotor to operate under a wider range of wind speeds without stall. It is noted that no engine was mounted on the wind turbine and the so-called operation conditions were driven simply by wind produced by a fan, as shown in Fig. 2. The fan can produce airflow with capacity up to 9300 m^3/h and wind speed up to 9.14 m/s. The 10-minute averages and reference along-wind turbulence intensity (T_u) of the generated wind speeds at the tower hub are presented in Table 5. It should be noted that the turbulence intensity is described as 'reference' because the temporal resolution of the anemometer is 1 Hz, which is insufficient to capture the turbulence behavior of the flow accurately.

Table 5. 10-minute averages and reference turbulence intensities (T_u) of the generated wind speed in the experiments.

Wind speed (m/s)	2.552	3.460	4.310	4.821	5.312	5.934	7.012
Reference T_u (%)	23.2	13.0	10.4	8.77	7.88	6.86	5.07

The base of the model was mounted on a shake table, which has the dimensions of 460 mm by 460 mm, a stroke of ±75 mm and an acceleration capacity of 2.5 g under a 7.5 kg load [56]. The shake table was not activated in this initial 'wind-only' experiment. The experimental set-up is described in Fig. 2. The accelerometers have a frequency range of 0.2 Hz – 2.5 kHz and a voltage sensitivity of 50.015 $mV/m \cdot s^{-2}$. They were set along the fore-aft and the side-side direction at the tower top. The digital anemometer has an effective range of 0 – 45 m/s and a sensitivity of ± (2.5%+0.1), which was used to measure the wind speed at the hub in real time. The rotor speed was also recorded during the experiment by means of a laser tachometer with an effective spectrum of 10 – 999 rpm and a sensitivity of ± (0.04%+2).

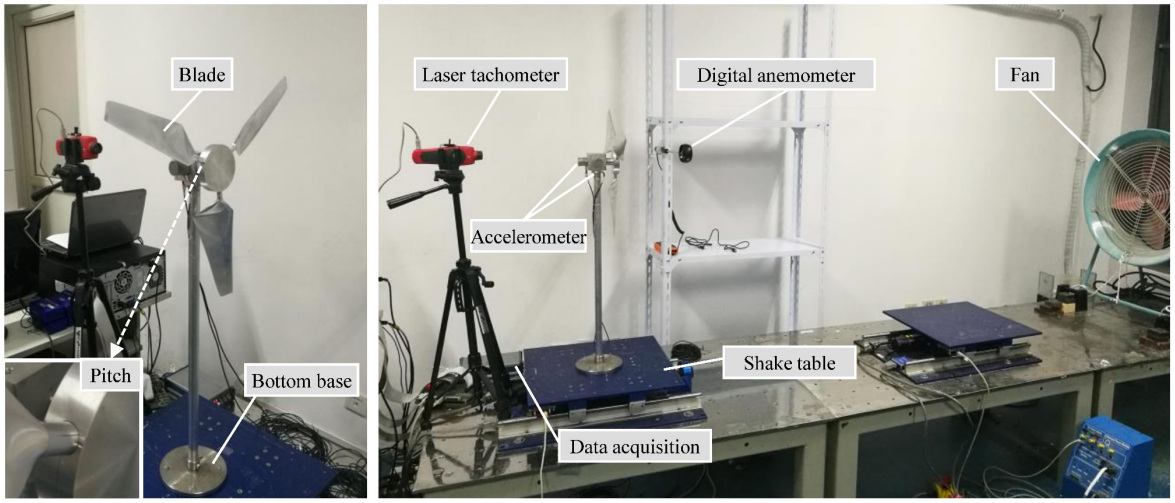

Fig. 2. Experimental setup.

3. Experimental validation of the methods to estimate the aerodynamic damping

In order to measure the structural frequencies and damping of the wind turbine model, the first tests were conducted without wind or earthquake actions applied. Pull-release tests in which an initial displacement of 5 mm was applied at the tower top in the fore-aft direction were performed with the blades remaining stationary. Free decay vibrations were recorded to estimate the dynamic properties of the model. The tests were repeated seven times and the arithmetic mean of the results yielded the following: fundamental fore-aft frequency 7.357 Hz and damping ratio 1.524%; fundamental side-side frequency 8.348 Hz and damping ratio 1.073%. The coefficient of variation (CoV) between tests was less than 4%. In the parameter extraction procedure, attention was paid on the orthogonal modal coupling. Taking as an example the results of one test included in Fig. 3, it is observed that the vibration in the side-side direction can be induced by the applied movement in the fore-aft direction, and the transfer of energy between two directions lasts until the model stops vibrating. Apart from this, the vibrations in two directions seem to be amplitude-modulated by a harmonic function (with a period of 0.97 s), which is known as beat phenomenon [57]. It is caused by the relatively close fundamental frequency in the two orthogonal directions of the slender cylindrical tower being tested. To obtain exponential decays in the local peaks of the responses, band-pass filters with 0.1 – 8 Hz and 8 – 15 Hz were applied to the original measurements of the fore-aft and the side-side acceleration time-histories, respectively. The 8-order Elliptic filter was utilized with a stop band ripple that is below -100 dB to avoid filtering out vibration signals that are of interest in this study. The filtered vibrations are shown in Fig. 3, where the beat phenomenon is no longer observed. Subsequently, the damping ratio can be calculated by exponential curve fitting to the envelope of the filtered signal as

$$x(t) = A_0 e^{-2\pi f_n \zeta t} \tag{1}$$

where A_0 is the acceleration amplitude, f_n is the fundamental frequency and ζ is the damping ratio.

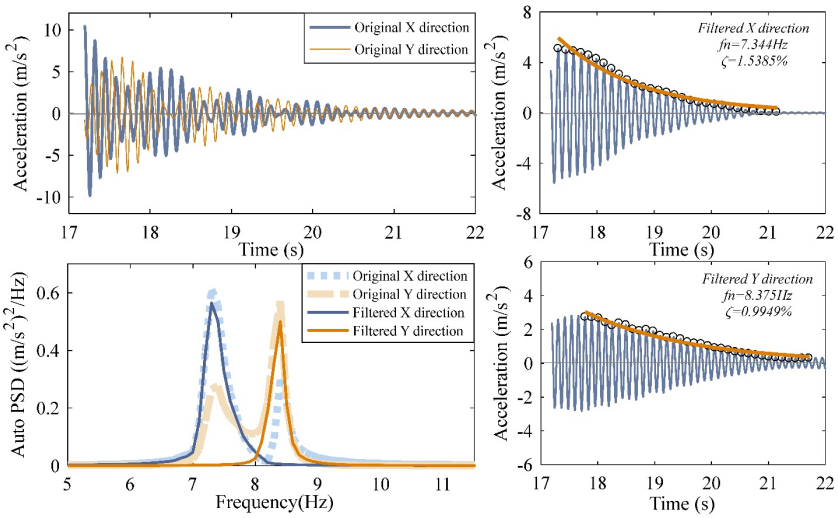

Fig. 3. Structural damping ratio estimates, where the initial displacement is imposed in the fore-aft direction (only). Sample frequency: 512 Hz. X direction is fore-aft; Y direction is side-side.

To evaluate the aerodynamic damping of the wind turbine model in operation, the blades were allowed to rotate simply by the wind action. Based on the rotor dynamic theory, an unbalanced rotor mass (m_r) with an eccentricity ε from the mass center induces harmonic excitations in the side-side direction defined as [58]

$$f(t) = \varepsilon m_r [\Omega(t)]^2 \sin[\Omega(t)t + \theta] \tag{2}$$

where Ω is the rotational frequency of the blades ($\Omega = 2\pi \times N/60$), and θ is the phase angle. Therefore, the recorded response signals have mixed contributions from the rotor and from the tower frequencies. Taking the wind speed of 7 m/s as an example. Fig. 4 presents the time-varying frequency content of the excitation, by converting each rotor speed reading to a rotational frequency (1 rpm = 1/60 Hz). For safety reasons, the fan was powered off once the rotor speed exceeded 900 rpm, which is responsible for the drop of the rotational frequency after approximately 20 s from the start of the test in Fig. 4. The tower-top acceleration in the side-side direction and the Hilbert energy spectrum derived from the recorded acceleration are shown in Fig. 5. By comparing Fig. 4 and the Hilbert spectrum in Fig. 5, it can be observed that the latter reproduces the harmonic action of the rotor (Ω_{max} =14.25 Hz) as well as the fundamental side-side mode of the tower (f_n=8.375 Hz). Fig. 5 also shows that resonance occurs when Ω approaches the fundamental frequency of the tower at the start and at the end of the test. Between these two stages (15 – 30 s) the rotational frequency is sufficiently separated from the natural frequency of the tower to show a clear frequency content. Therefore, in this period it is possible to extract the fundamental vibration mode of the structure under the influence of the wind-structure interaction by filtering out the excitation frequency components. To this end, a 0.1 – 8 Hz band-pass filter was applied to the tower top acceleration records in the fore-aft direction and an 8 – 10 Hz filter in the side-side direction. The auto-correlation function was then computed through the inverse Fourier transform of the power spectral density of the filtered signal [59]. The exponential curve fitting Eq. (1) was subsequently applied to the auto-correlation function to extract the total damping (c_{tot}), from which the component due to the aerodynamic damping (c_{aero}) can be estimated by subtracting the structural damping (c_{st}), as shown in Fig. 6. The total damping coefficient is defined as

$$c_{tot} = 2m\omega\zeta \tag{3}$$

where m denotes modal mass of the fundamental vibration mode (calculated as 1.2248 kg in the fore-aft direction and 1.2209 kg in the side-side direction in the proposed structure).

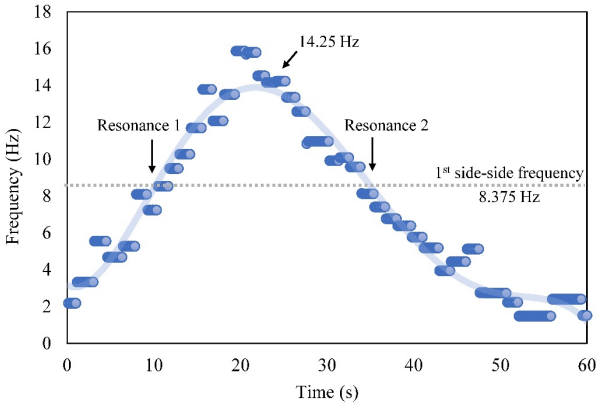

Fig. 4. Rotational frequency of the blades.

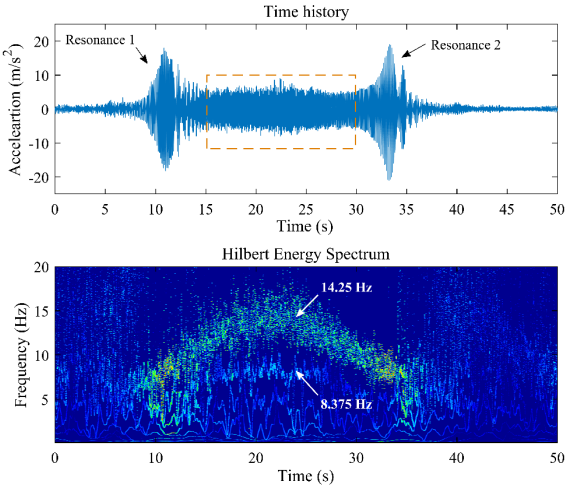

Fig. 5. Accelerogram and time-frequency analysis of one of the side-side acceleration measurements. Wind speed: 7m/s.

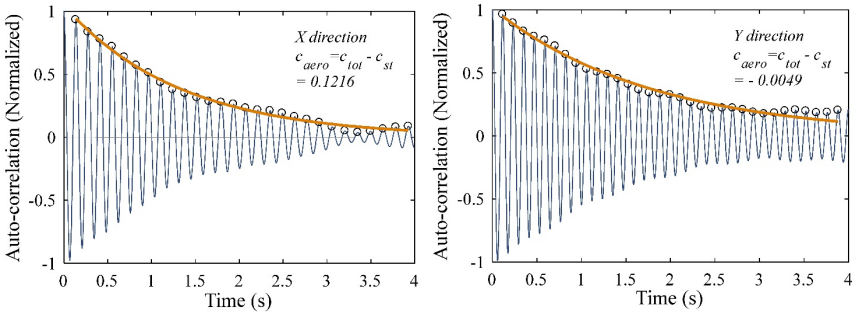

Fig. 6. Estimation of the aerodynamic damping coefficients. X refers to the fore-aft direction; Y refers to the side-side direction. Wind speed: 7m/s. Rotor speed: 855 rpm. Sample frequency: 512 Hz.

Given the operational conditions, the blade geometry and the aerodynamic characteristics of the turbine model, the aerodynamic damping can be estimated following the methodology shown in Fig. 7. The methodology is based on the BEM theory with the Prandtl's tip/root loss factor described in Section 2 and with the Glauert correction. The latter applies to situations when the axial induction factor (a) exceeds the valid range for the BEM theory ($a < 0.4$ in this paper) [4]. Table A.1 shows a certain case of wind/rotor speed ($V_W = 7$ m/s and $N = 855$ rpm) following the method of Valamanesh and Myers [32] and the method of Kühn [35] which were already introduced in Table 1. A total of 6 cases with different wind/rotor speeds were analyzed in this work. Fig. 8 presents the comparison between the aerodynamic damping coefficients measured experimentally and those calculated using different methods. The size of the markers in this plot is related to the magnitude of the aerodynamic damping coefficient. The effect of the increase in the pitch angle (manually adjusted) is also included in this study at the wind speeds of 2.5 m/s and 7 m/s. Its influence on the rotor speed and on the aerodynamic damping is indicated by the white arrow in Fig. 8 (from pitch angle 0° to 15°).

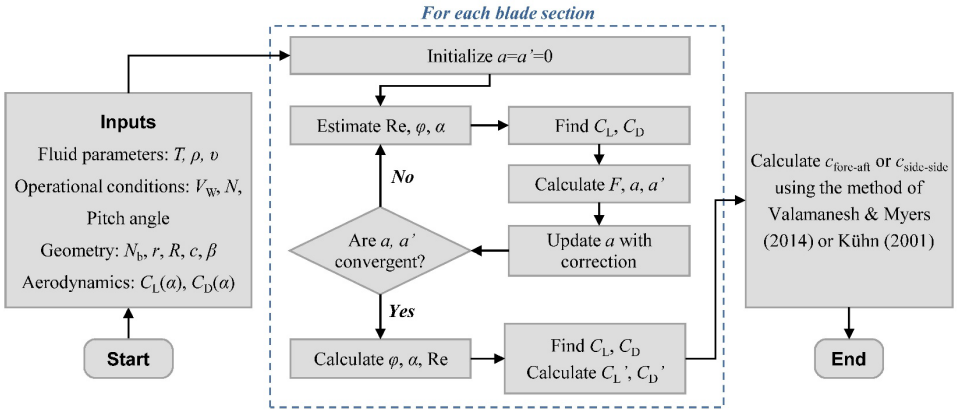

Fig. 7. Methodology to calculate the aerodynamic damping coefficients.

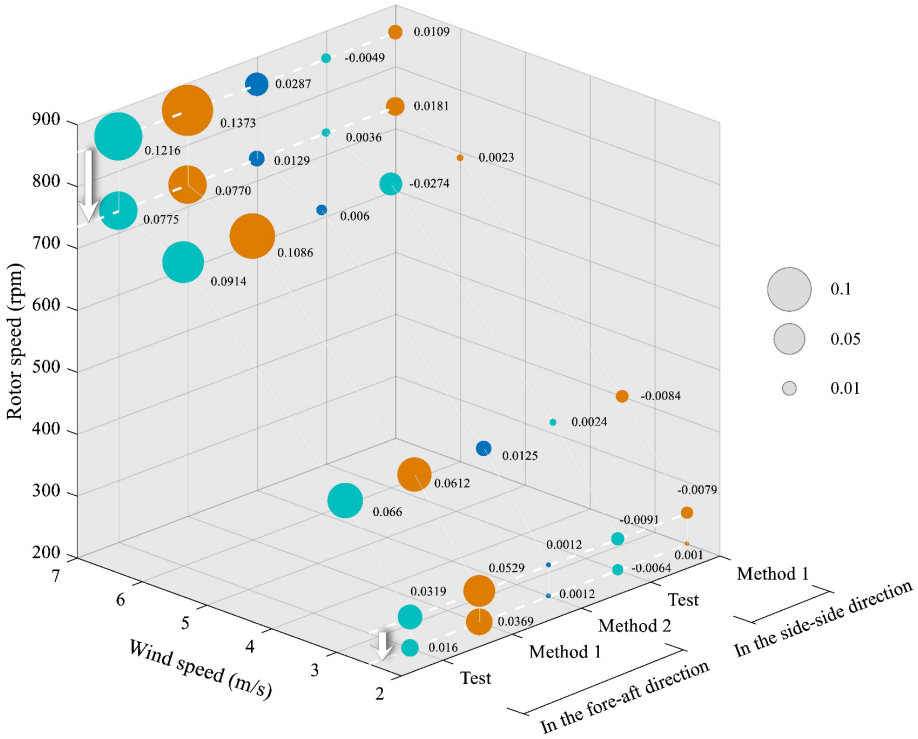

Fig. 8. Comparison between the aerodynamic damping coefficients measured experimentally and the calculated ones. Nomenclature: 'Test' refers to the experimental measurement; 'Method 1' is the method of Valamanesh and Myers [32]; 'Method 2' is the method of Kühn [35].

The results in Fig. 8 indicate that:

1) The fore-aft aerodynamic damping coefficient increases with the wind speed. This can be explained by the large contribution of the rotor speed to the fore-aft aerodynamic damping. The higher the wind speed, the faster the rotor spins, and thus the larger the fore-aft aerodynamic damping, which is consistent with previous works (see Table 1). In addition, increasing the pitch angle (from 0° to 15°) can effectively slow the rotor speed and thereby decrease the fore-aft aerodynamic damping.
2) It can be observed that the aerodynamic damping in the side-side direction is much smaller than that in the fore-aft direction, which can be explained with the wind load diagram on the blade shown in Fig. 9. The vector sum of the lift (L) and the drag (D) at a particular blade section, R_f, can be decomposed into the normal and the tangential forces F_N and F_T, respectively. To assess the resultant dynamic behavior of the tower, the forces in the local blade (rotating)

coordinates (x'-y'-z') need to be transformed into the global (fixed) coordinates at the tower top (x-y-z) as

$$F_x = F_N, F_y = F_T \cos(\gamma(t)) \tag{4}$$

where γ denotes the azimuth of the blade with respect to the axis z. The alteration of F_N or F_T induced by the tower-top motion can be regarded as the aerodynamic damping force. The aerodynamic damping forces at the three blades are aligned all the time in the fore-aft direction. However, in the side-side direction, they are influenced by the rotation of the blades and the aerodynamic damping forces tend to cancel each other, with the consequent reduction of the resultant damping force at the tower top.

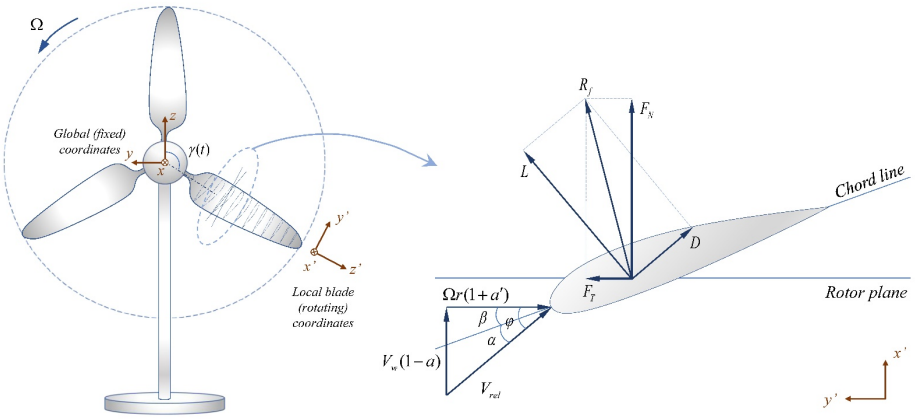

Fig. 9. Local velocities and loads on a blade section.

3) The method proposed by Valamanesh and Myers [32] (Method 1 in Fig. 8) yields estimates of the aerodynamic damping that are closer to the experimental observation than those obtained from the method suggested by Kühn [35] (Method 2). Referring back to Table 1, Kühn's model is actually a particular form of Valamanesh and Myers's model valid for small inflow angles (it assumes $\cos\varphi \approx 1$), attached flows around the blade sections ($C_L \gg C_D$) and high tip speed ratios ($\Omega r \gg V_W$). The wind turbine model in this paper does not adhere to the aforementioned assumptions and for this reason Kühn's method is not applicable. For example, the inflow angle (φ) is not negligible according to the results presented in Table A.1. The Valamanesh and Myers's model seems to be more applicable in this work and it can capture the relationship between the wind speed and the aerodynamic damping effect.

The disagreement between the aerodynamic damping coefficients measured experimentally and those obtained from the calculation proposed by Valamanesh and Myers [32] can be attributed to:

1) Measurement uncertainties of the wind speed and the rotor speed. This influence is relatively small since it can be suppressed by the application of measurement facilities with relatively high resolution and by repeated tests.
2) Errors in the estimation of the structural damping and the total damping. Two different approaches were adopted to improve the effectiveness of the damping estimates in this work. The first one was to increase the sampling time of the vibration signals for the test and the second to increase the number of tests. The quantity selected to calculate the structural damping is $\omega\zeta$ because it results directly from the curve fitting of the envelope of the time-domain responses. The tests were repeated seven times in the estimation of $\omega\zeta$ and the results gave a very stable estimate of this quantity, with a CoV between tests that is below 1%. For the estimation of the total damping with wind speeds of 2.5 m/s and 3.5 m/s, the sampling time for the experiment was set to 600 s and the Welch's averaged periodogram method was adopted to estimate the power spectral density with fine frequency resolution (0.03125 Hz) and low noise level to obtain accurate damping estimates. It should be mentioned that the test was not repeated for the cases with wind speeds of 2.5 m/s and 3.5 m/s. For the estimation of the total damping with wind speeds of 6 m/s and 7

m/s the spectral analysis was also used to estimate the damping, however, as it is shown in Fig. 5, the occurrence of resonance limited the sampling time. In order to evaluate the reliability of the estimation with shorter sampling time with resonant wind speeds, the tests were repeated five times for the case with 7-m/s wind speed (with 855-rpm rotor speed and 0º pitch angle), which gave a CoV in the damping estimate of less than 2%. The error propagation analysis for this specific case is presented in Table A.2 in the Appendix. It was found that the uncertainty (standard error) of the total damping is 2 – 3 times larger than that of the structural damping, which is mainly due to the uncertainty introduced from the spectral estimation process. It was also observed that the aerodynamic damping calculated with the method of Valamanesh and Myers [32] overlaps with that estimated through the experiments. This further supports the observation that this method tends to give good estimates of the aerodynamic damping.

3) Inconsistencies in the T_u of the wind field generated by the wind tunnel in the literature [44] and by the fan in this study. The aerodynamic performance of the airfoil is sensitive to the free-stream turbulence and the omission of T_u effect is regarded as a major source of error. T_u is measured as about 5% at wind speed of 7 m/s in this study, which is much higher than that measured experimentally by McArthur [44], where $T_u < 0.03\%$. No information is given in previous research works about the influence of T_u for the E387 airfoil, but the influence can be inferred from other low-*Re* airfoils. For the NACA 0012 airfoil, a 51%-increment in the maximum of C_L was reported as T_u was increased from 0.6% to 6.0% at Re = 5,300, whereas only 12%-increment was observed at Re = 20,000 [60]. It can be found that the effect of T_u is limited and weakened when *Re* reaches the order of 10^4 [61]. Therefore, it is considered admissible to apply McArthur's results [44] in the aerodynamic damping calculation in this work.

4. Experimental study on the interaction of the wind-seismic response

In this section, the combined response of the turbine under wind and seismic actions is studied. The wind flow was produced by the fan with an average wind speed of 2.5 m/s and the average rotor speed of the turbine model was measured as 250 rpm. The shake table only allowed to apply the earthquakes in the fore-aft direction, parallel to the wind flow. The accelerations at the top of the tower were recorded by the orthogonal set of accelerometers described previously, and the input accelerations at the base of the tower were recorded by three accelerometers installed on the table. A combination of natural and synthetic earthquakes was considered in this study. The artificial ground motion (labeled as EQ1) was generated based on the design spectrum proposed by the Chinese seismic code [62] with a characteristic period of the soil of 0.4 s (similar to Soil Class C in ASCE/SEI 7-10 [31]). Three recorded ground motions were selected from the PEER Database [63]. These are the earthquakes of El Centro (Year: 1940, Station: Array # 9, labeled as EQ2), Taft (Year: 1952, Station: Lincoln School, labeled as EQ3) and Kobe (Year: 1995, Station: Takarazuka, labeled as EQ4). These four ground motions were all time-scaled (with a scale ratio of 0.0707) to reproduce the seismic response characteristics of a 1.5-MW onshore wind turbine. In addition, each of the earthquakes was amplitude-scaled to 0.4*g* and 0.8*g* peak ground acceleration (PGA). For EQ1 PGA intensities of 0.2*g* and 0.6*g* were also applied. The elastic response spectra were calculated for the ground motions considering 1.5-% damping, which is in line with the value observed in Section 3. The four scaled spectra are presented in Fig. 10 along with the design spectrum. Each ground motion was repeated three times, with and without wind. In the tests with wind, the earthquake motion was applied after a certain amount of time (about 50 s) to dissipate the transient behavior induced by the wind. A total of 30 tests were performed to measure the seismic response (without wind), with 30 additional tests conducted to obtain the combined response including wind and earthquake excitations.

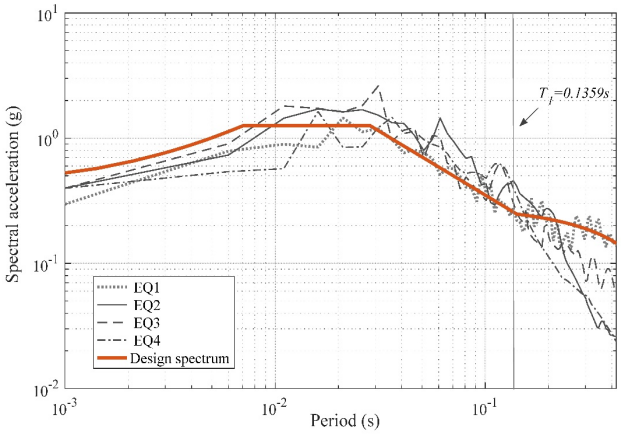

Fig. 10. Spectral acceleration for the applied ground motions obtained with 1.5% damping (PGA = 0.4*g*).
The vertical line represents the fundamental period of the model in the fore-aft direction (T_1 = 1/7.357 = 0.1359s).

The analysis of the response for EQ2 (PGA = 0.4*g*) in the time and frequency domains is illustrated in Fig. 11. The response recorded by the accelerometer set in the fore-aft direction contains the contribution of the side-side vibration mode, which is the result of the orthogonal modal coupling discussed in Fig. 3. It is worth mentioning that the natural frequencies of the two modes in Fig. 11 are slightly different from those estimated in the free-vibration test in Fig. 3 (7.375 Hz vs. 7.344 Hz in the fore-aft direction and 8.5 Hz vs. 8.375 Hz in the side-side direction) because of the different frequency resolutions selected in the signal post-processing. It is found that in the presence of seismic motions, when the wind is applied at the blades the tower-top response in the fore-aft direction is slightly smaller compared to that of the earthquake-only scenario. The interaction between the aerodynamic and the earthquake actions is responsible for the reduction of the response. Although the wind flow and the ground motions were not directly oriented in the side-side direction, the response in this direction was also reduced by the wind. This could be attributed to the twist introduced along the blades as a result of their optimization process (see Fig. 1), which introduces side-side wind components.

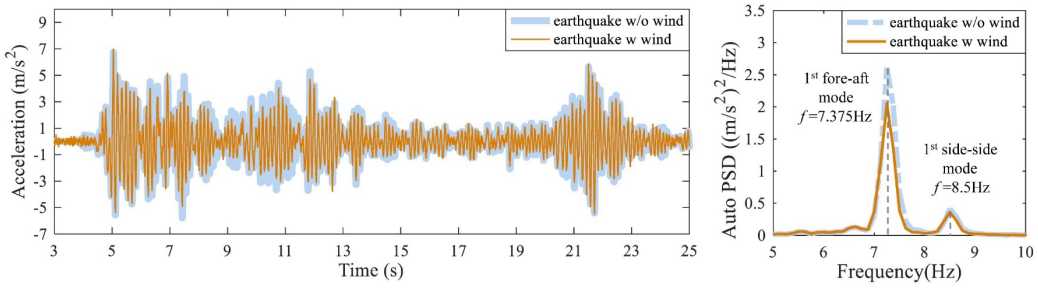

(a) fore-aft direction

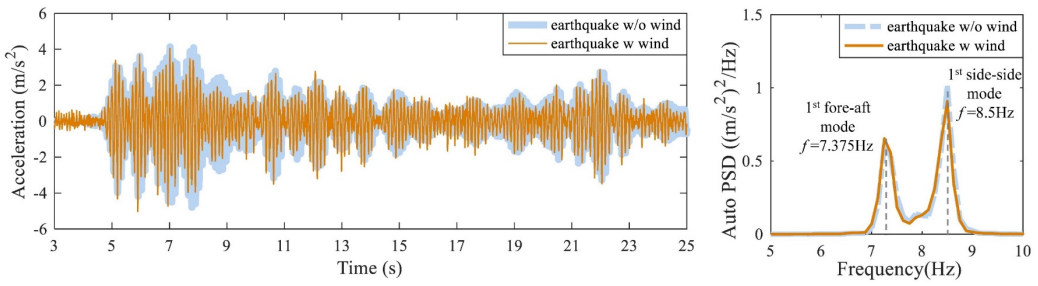

(b) side-side direction

Fig. 11. Tower top acceleration responses under earthquake excitations with/without wind loads in time and in frequency domains.
EQ2 with PGA = 0.4*g* was applied in the fore-aft direction. Sample frequency: 256 Hz.

The peak accelerations associated with the fore-aft mode in the frequency-domain for the earthquake-only, the wind-only and the coupled wind-seismic cases are 1292.2 mm/s^2, 86.0 mm/s^2 and 1243.7 mm/s^2, respectively. This yields an 11% difference (obtained as (1292.2 + 86.0 – 1243.7)/1243.7) between the simple sum of the wind-only and the earthquake-only responses, compared with the actual response with wind and earthquake actions applied at the same time. This is attributed to the fact that the change of the flow velocity on the blades due to the ground motion will not affect the aerodynamic loads instantaneously but with a certain delay [4]. In other words, the peak response under separate wind and seismic loads do not necessarily occur at the same time. Therefore, adding directly the wind and the earthquake-induced maxima is a conservative estimate.

A practical approach to combine the wind and the earthquake loads was investigated. To this end, the experimental results were analyzed and compared with those obtained from different methods recommended in design guidelines and in previous research works. To facilitate the discussion, a wind-seismic combination coefficient is proposed as

$$\eta = \frac{R(E,W)}{R(E)+R(W)} \tag{5}$$

where $R(\cdot)$ represents the responses obtained when the earthquake and the wind are applied simultaneously (E,W), when only the earthquake is applied (E) or when only the wind is applied (W). These responses are expressed as the peak values in the time-domain (referred as 'T-p'), the root mean square (rms) of the responses in the time-domain ('T-rms'), and the peak responses associated with the fore-aft mode in the frequency-domain ('F-p'). The response T-p focuses on the transient behavior of the turbine; T-rms on the stability of the response; and F-p on the vibrations controlled by the fundamental fore-aft mode. In all the cases the response measure is the acceleration at the tower top in the fore-aft direction in m/s^2. The resulting combination coefficients are presented in Fig. 12. An apparent outlier was excluded for PGA = 0.6g in EQ1 because of a test failure. Although there exists some record-to-record variability of η for different response indicators, they share the same trends and almost all of them fall between 0.75 and 1. It should be mentioned that the coefficient η = 1 is recommended by IEC 61400-1 [22] and GL [23], and it represents a direct additive combination, whereas the coefficient η = 0.75 is recommended for large-scale wind turbines by ASCE/AWEA [13] as a load reduction factor. The experiments suggest that η = 1 is an over-conservative combination rule. In light of the scale of the model in this study, the aerodynamic loads are limited and the earthquake responses make the largest contribution. This explains that the resulting combination coefficients in this work are above 0.75. No clear correlation was observed between the combination factors and the PGA, although η seems to increase slightly for stronger earthquakes because of the larger contribution of the seismic action. It's worth mentioning that no damage was observed in the tower due to the seismic actions, even with the largest PGA.

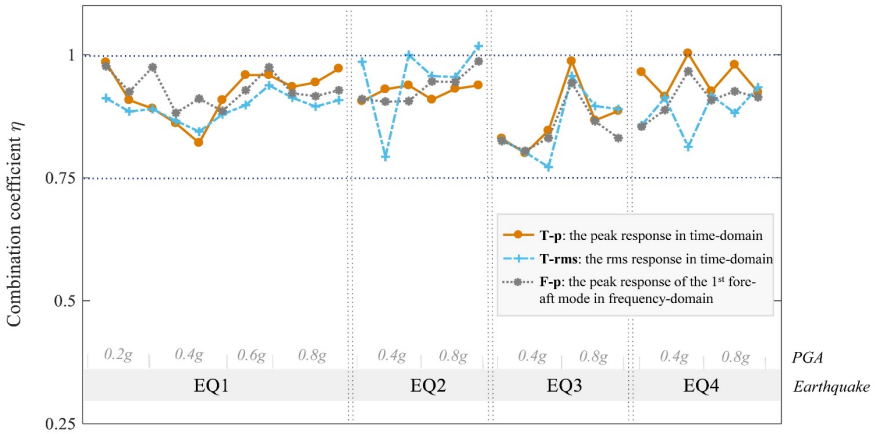

Fig. 12. Combination coefficients with different assessment indicators.
The response refers to the acceleration at the tower top in the fore-aft direction.

Additionally, the SRSS combination proposed by Prowell [14] was examined and compared with the combination factor η = 0.75. The error is defined as

$$e = \frac{R_{combined} - R_{ref}}{R_{ref}} \tag{6}$$

where R_{ref} represents the experimental response corresponding to simultaneous action of wind and earthquakes, which is taken as a reference, and $R_{combined}$ is the result calculated from the combination of separate wind and earthquake responses with different methods defined as

$$R_{combined} = \begin{cases} 0.75\big(R(E) + R(W)\big), & \eta = 0.75 \text{ method} \\ \sqrt{R(E)^2 + R(W)^2}, & \text{SRSS method} \end{cases} \tag{7}$$

where the F-p response indicator is selected for the values of $R(E)$ and $R(W)$ to avoid the scatter introduced by peaks of the acceleration in the time-domain. Fig. 13 shows these results and it indicates that the SRSS method usually gives results that are larger than the experiments, and η = 0.75 typically leads to lower responses. This is attributed to the relatively large difference between the earthquake and the wind responses, with the former tending to dominate the SRSS results. Moreover, the ground motions for which η = 0.75 increases the error are associated with the improved accuracy of the SRSS method. The SRSS combination (peak error 14%) tends to provide better estimates compared to η = 0.75 (peak error -24%). This finding, however, should be further explored in larger-scale wind turbines in which the aerodynamic loads are expected to contribute more to the combined wind-seismic response.

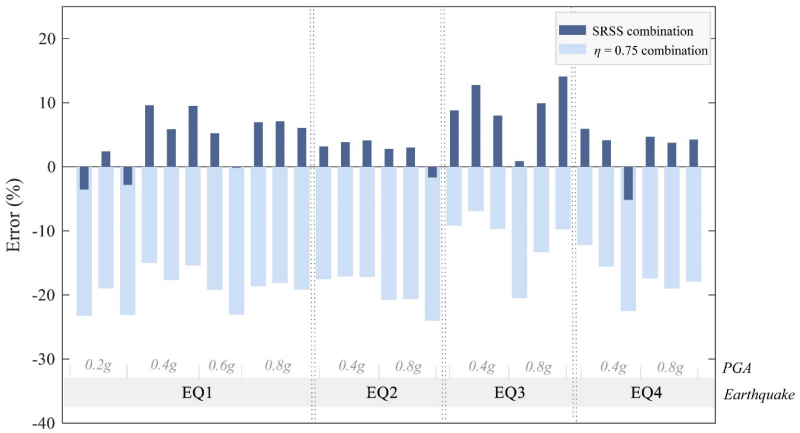

Fig. 13. Deviation of the SRSS and η = 0.75 combination methods with respect to the experimental results.

5. FAST simulation results

Considering the stochastic nature of the wind and earthquake actions as well as the limited aerodynamic effects that can be developed in the experimental testing of the 1/100-scaled turbine model, the study in Section 4 is complemented here with series of simulations under different combinations of the wind speed and the PGA. The numerical platform FAST [19] was employed for the dynamic response simulation of the wind turbine by means of a fully-coupled aeroelastic analysis under simultaneous wind and earthquake actions. The FAST simulation follows the analysis flowchart presented in Fig. 14.

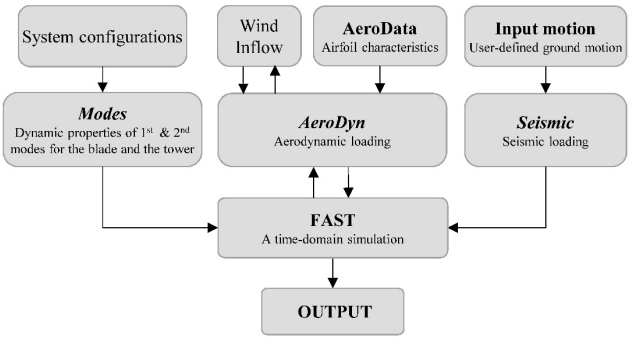

Fig. 14. Flowchart of FAST [19].

FAST allows to describe the dynamic properties of the tower and the blades by introducing the first two vibration modes of the tower in the fore-aft and side-side directions, along with first flapwise and edgewise modes of each blade, as illustrated in Fig. 15. The natural frequencies of the numerical model were adjusted based on the results obtained experimentally in the testing presented in Section 3. A wind field covering the entire area of the rotor disc as well as the tower was generated with the mean wind speed and the turbulence intensity according to Table 5. The aerodynamic coefficients of the E387 (Re = 20,000) for the full range of angles of attack (from -180° to 180°) are presented in Fig. 16, which were introduced in the FAST model. To calculate the aerodynamic actions on the blade, the BEM theory with the Prandtl's tip/root loss factor and the Glauert correction mentioned previously was adopted. FAST also captures the dynamic stall effects, and therefore, it is more accurate than the BEM theory employed in the methods proposed by Valamanesh and Myers [32] and by Kühn [35] that were discussed in Section 3. The accelerations recorded at the shake table were imposed at the tower base in the dynamic analysis, along with the rotor speeds that were measured experimentally. With all the information, a time-domain simulation incorporating the interaction between the aerodynamics and the structural dynamics of the turbine model was conducted to obtain the response.

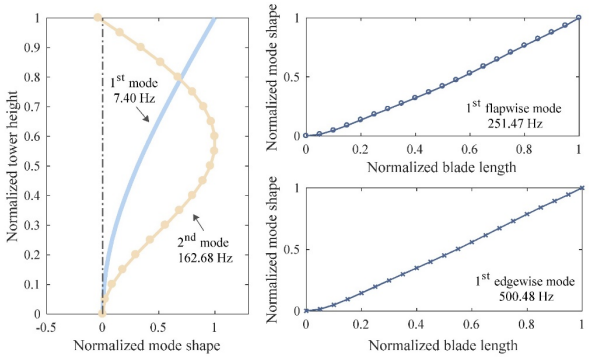

Fig. 15. Normalized mode shape of the tower and the blades.

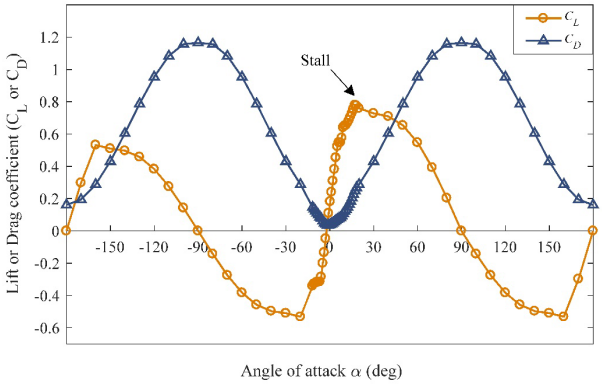

Fig. 16. Aerodynamic coefficients for the full range of angles of attack. Re=20,000.

5.1 Discussion about the wind field in the experiments and in the numerical analysis

In order to validate the wind field generated by the fan in the experiments, a series of simulations were conducted in FAST using only wind actions obtained from a code-defined (IEC 61400-1 [22]) boundary layer profile accounting for time- and spatial correlations of the wind speeds at different points of the structure, and scaling it up to 6 different intensities (with/without the adjustment of pitch angle) which are consistent with the cases in Fig. 8. Fig. 17 presents the comparison between the wind responses in the fore-aft direction calculated from FAST and the recorded ones in the experiments. Three response indicators are defined following Eq. (5). It was found that the responses obtained from the simulation give results that are close to the experimental ones except for the 'T-p' response with the 6-m/s wind speed. These results confirm the validity of the wind field generated in the experiments for the purposes of this work.

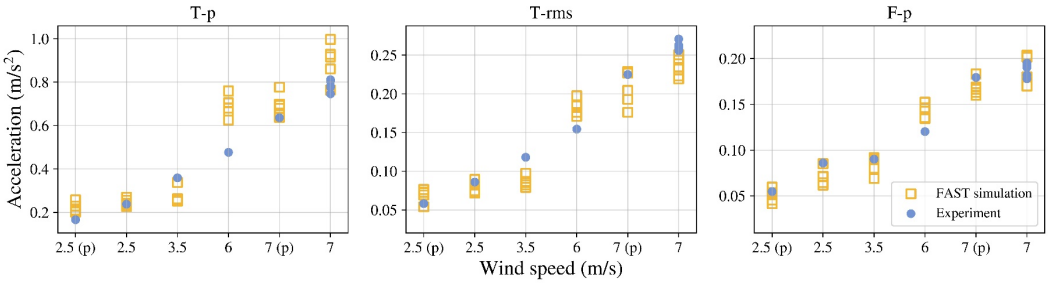

Fig. 17. Comparison between the wind responses in the fore-aft direction calculated from FAST and the recorded ones in the

experiments. '(p)' in the horizontal axis represents the adjustment of the pitch angle of blades from 0º to 15º.

5.2 Wind and earthquake effects

Apart from earthquakes of El Centro (EQ2), Taft (EQ3) and Kobe (EQ4), seven additional recorded ground motions were selected from the PEER Database. Each ground motion was time-scaled with a scale ratio of 0.0707. The description of the ground motions' ensemble is listed in Table 6 and their spectral accelerations are presented in Fig. 18. The PGA of the 10 natural ground motions and the artificial one (EQ1) was scaled to 0.1g, 0.2g, 0.4g, 0.6g, 0.8g and 1.0g without changing their frequency content. Each ground motion was applied to the turbine model in FAST in the fore-aft direction with four different wind speeds (2.5 m/s, 3.5 m/s, 6 m/s and 7 m/s), and each wind inflow was repeated five times with different random phases in the wind time-histories to consider the stochastic nature of the wind, which resulted in 11 × 6 × 4 × 5 = 1320 simulations. The earthquake motion was applied in the analysis after 50 s to dissipate the transient response. The simulations were also conducted for ground motions under different PGAs without wind, which gives 11 × 6 = 66 additional runs.

Table 6. Selected recorded ground motions for simulations

Number	RSN	Year	Event	Station	Magnitude	
1	6	1940	Imperial Valley-02	El Centro Array #9	6.95	EQ2
2	7	1941	Northwest Calif-02	Ferndale City Hall	6.6	
3	12	1952	Kern County	LA - Hollywood Stor FF	7.36	
4	15	1952	Kern County	Taft Lincoln School	7.36	EQ3
5	17	1952	Southern Calif	San Luis Obispo	6	
6	26	1961	Hollister-01	Hollister City Hall	5.6	
7	40	1968	Borrego Mtn	San Onofre - So Cal Edison	6.63	
8	68	1971	San Fernando	LA - Hollywood Stor FF	6.61	
9	77	1971	San Fernando	Pacoima Dam	6.61	
10	1119	1995	Kobe_ Japan	Takarazuka	6.9	EQ4

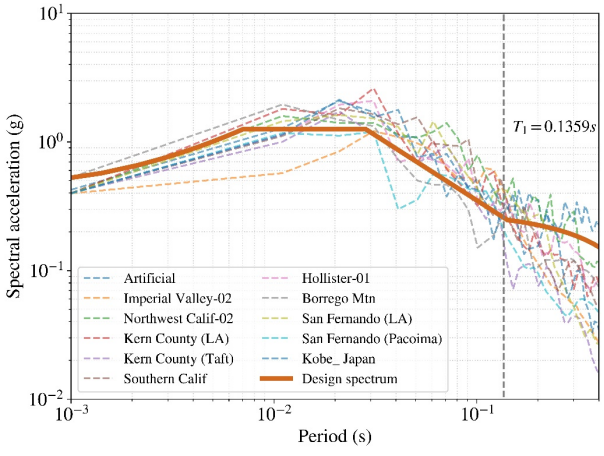

Fig. 18. Spectral acceleration for the applied ground motions obtained with 1.5% damping (PGA = 0.4g). The vertical line represents the fundamental period of the model in the fore-aft direction (T1 = 1/7.357 = 0.1359s).

The numerical responses under simultaneous wind and earthquake actions also compare well with the experimental ones, as it is illustrated in Fig. 19. The discrepancies of the response in the time-domain (up to 13.81% difference in T-p and 11.86% in T-rms) can be explained in the frequency-domain, where the side-side mode component contributes in

the fore-aft response of the tower due to orthogonal modal coupling. This phenomenon is much stronger in the experimental results and it results in the reduction of the amplitude of the fundamental fore-aft mode vibration. The contribution of the second fore-aft mode of the tower can be evaluated by analyzing the acceleration recorded at the middle point of the tower. As shown in Fig. 20, the second fore-aft mode (163 Hz) seems to be submerged in the noise, and it has no appreciable influence on the tower response. Therefore, it is reasonable to consider the turbine model as a two-directional SDOF system (the fore-aft/side-side direction) in the aerodynamic damping calculation in Section 3.

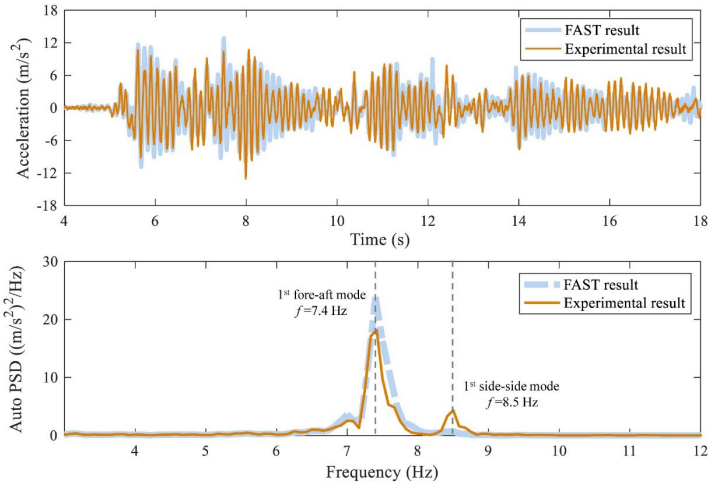

Fig. 19. Comparison of tower top acceleration in the fore-aft direction obtained in the FAST simulation and in the experiment. The earthquake EQ2 (PGA = 0.8*g*) and a 2.5 m/s wind speed are simultaneously applied in the fore-aft direction. Rotor speed: 250 rpm.

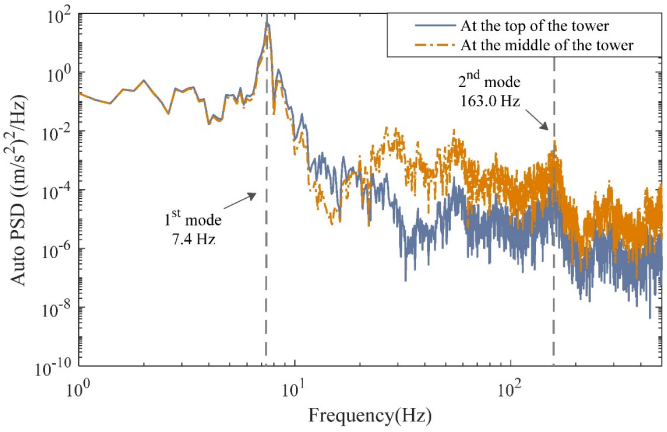

Fig. 20. Comparison of the accelerations recorded at the tower top and at the middle of the tower, both in the fore-aft direction.

After all the simulation cases, 1320 wind-seismic combination coefficients (η) were obtained for each response indicator, which are illustrated in Fig. 21. Based on the statistical analysis of these simulations, it is found that:

1) The value of η tends to decrease with the wind speed. This makes sense since higher wind speeds correspond to larger aerodynamic damping effect and therefore, contributing to a more significant wind/earthquake coupling effect.
2) The value of η increases with the PGA, but above 0.6g it is almost insensitive to this intensity measure. This can be explained by the fact that the contribution of the earthquake excitation is dominant for larger values of the PGA.
3) The dispersion of the estimate of η for the indicator 'T-p' is generally smaller than that for the indicators 'T-rms' and 'F-p'. Therefore, it is recommended to use 'T-p' when assessing the dynamic behavior of wind turbine structures by means of the simplified decoupled wind/earthquake method.

The simulations are also compared with the experimental results in Fig. 22 for the cases of the artificial ground motion (EQ1). It can be found that the value of η that is obtained from the simulation is close to the experimental one, except for the case with PGA of 0.4g.

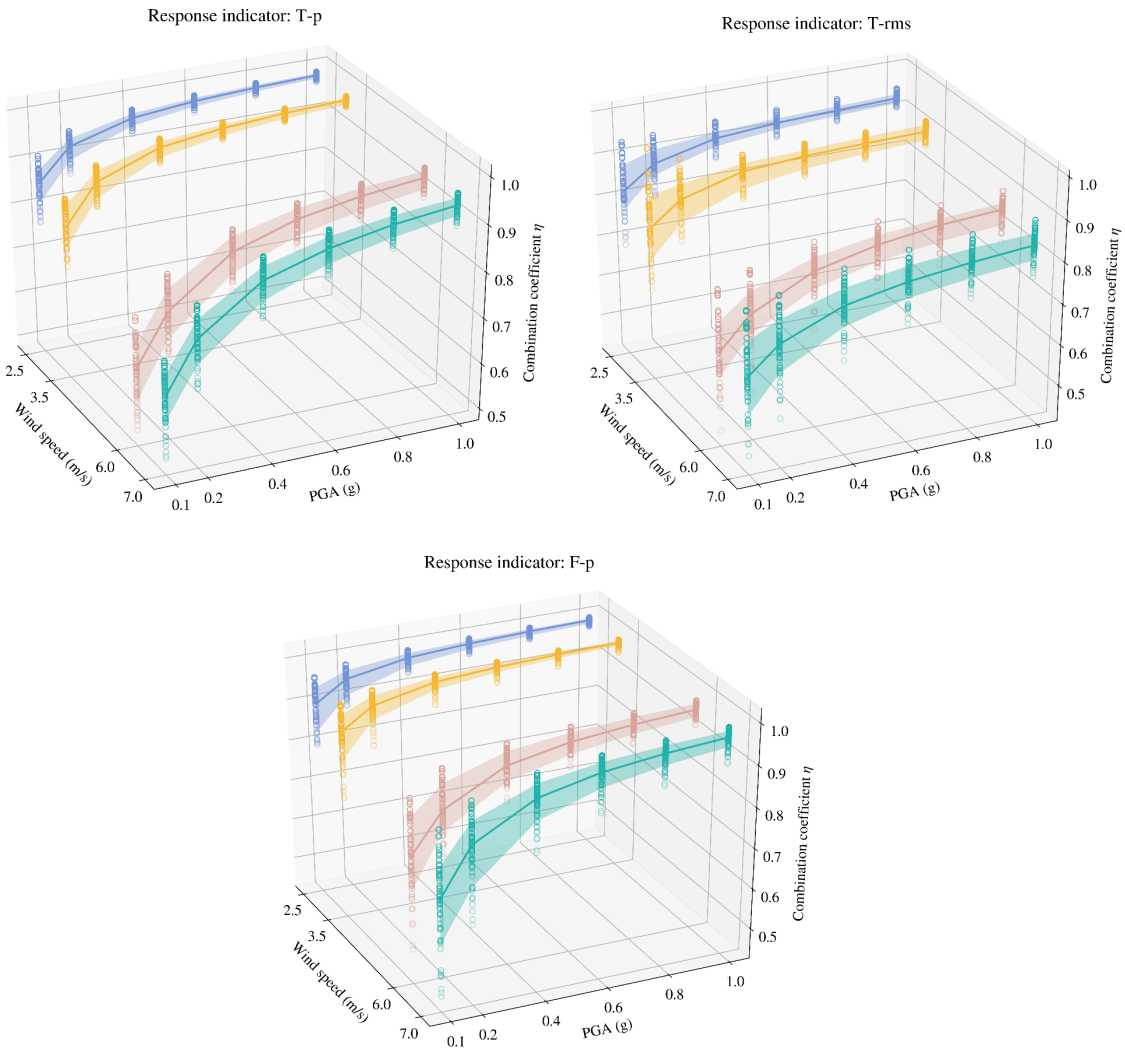

Fig. 21. Combination coefficients with different assessment indicators.

The response refers to the acceleration at the tower top in the fore-aft direction. Each column contains a group of 55 points which represent 55 simulation results of the model under a specific wind speed and PGA. The solid line represents the variation of the median value of each points group of results with the PGA. The filled area represents the variation of the range between the 16th and 84th percentile of each points group with the PGA.

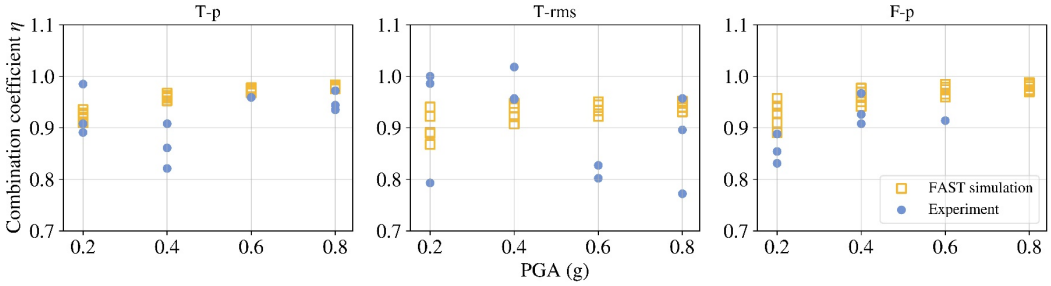

Fig. 22. Combination coefficients obtained from the experiment and the FAST simulation.

Ground motion: EQ1. Wind speed: 2.5 m/s.

It has also been observed that the magnitude of the wind-induced response compared with that caused by the ground motion affects the effectiveness of the load combination method directly. The relatively large number of simulations allows to further explore the adequacy of different load combination methods. Fig. 23 presents the deviation of the SRSS and the $\eta = 0.75$ combination methods with respect to the fully-coupled results obtained from the experiment and

from the FAST simulation under different wind/seismic response ratios. The response indicator 'T-rms' is selected to calculate the ratio for its ability to describe the effective value of the signal. The results indicate that:

1) The SRSS method tends to overestimate the fully-coupled response, and the $\eta = 0.75$ method to underestimate the result, which is consistent with the findings of Fig. 13.
2) The error of the SRSS method decreases with the wind/seismic response ratio and the error of the $\eta = 0.75$ method tends to be around -10% (i.e. it gives smaller values than the fully coupled analysis).
3) For extremely small wind/seismic response ratios, below 0.05, the seismic excitation dominates the total response and, in this case, there is no need to consider the coupling effect of the two actions, as shown in Fig. 23. However, when the wind/seismic response ratio is above 0.3 the dispersion of the error with both approaches is too large to provide reliable results. This figure indicates that for moderate wind/seismic response ratios (in the order of 0.05 – 0.3) the SRSS method can give estimates of the fully coupled wind-seismic response that are reasonably on the safe side, whereas the $\eta = 0.75$-method clearly underestimates the response.

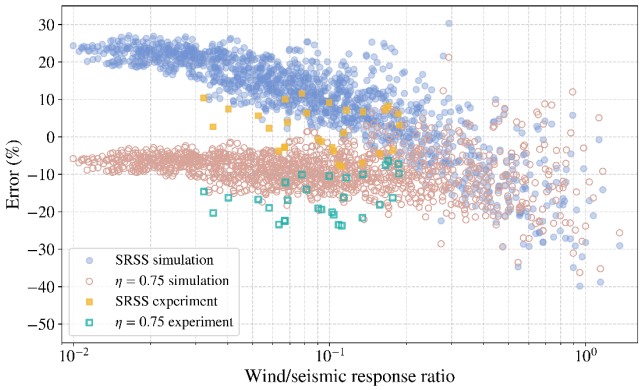

Fig. 23. Deviation of the SRSS and $\eta = 0.75$ combination methods with respect to fully-coupled results obtained from the experiment and from the FAST simulation. The response indicator 'T-rms' is used here.

The experimental work discussed in Section 4 only applied fore-aft ground shakings to the turbine model. Further investigation was undertaken with FAST to compare between the responses with shaking in the fore-aft and the side-side directions. The earthquake was applied independently in the two directions, and a 2.5 m/s wind speed was applied simultaneously with the earthquake in the fore-aft direction. Fig. 24 shows the results and it indicates that the peak amplitude in the fore-aft direction when the wind is considered is reduced by 6% in comparison with the case with only earthquake in the fore-aft direction, whereas no appreciable reduction can be observed when the earthquake is applied in the side-side direction. This difference demonstrates that the wind and the earthquake-induced responses interact in the fore-aft direction but not in the side-side direction. The result is in agreement with the experimental findings in Fig. 11 and with the experimental work of Prowell et al. [33].

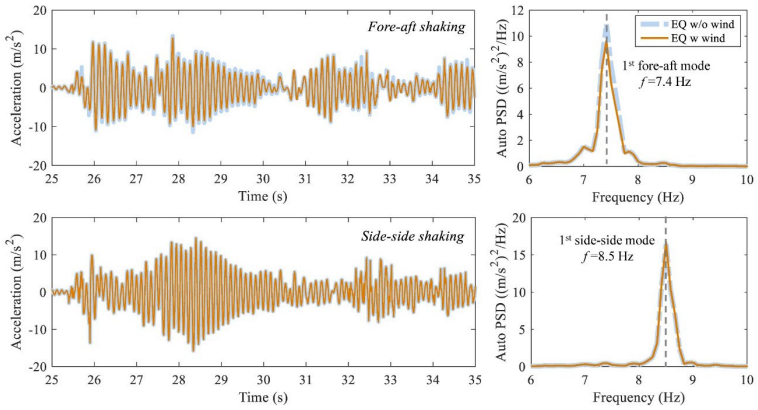

Fig. 24. Tower top response obtained in FAST with EQ2 (PGA = 0.8g) shaking applied independently in the fore-aft and in the side-side directions. The earthquake is applied simultaneously with a 2.5 m/s wind speed in the fore-aft direction.

Conclusions

In this research, a 1/100-scaled model of a wind turbine tower with optimized blades has been tested under simultaneous operational wind and earthquake actions. The goal was to investigate a practical approach to estimate the responses of wind turbine towers by analyzing both actions separately. A detailed blade design was conducted to ensure the aerodynamic performance under the condition of low Reynolds number. The evaluation of the aerodynamic damping in the tower response was first carried out by comparing the structural response in free vibration and under wind actions without ground motions. Afterwards, the interaction between seismic and wind loads on the wind turbine response was investigated experimentally by means of a shake table testing, and also numerically by means of dynamic FAST simulations. The main conclusions are the following:

1) The interaction between the structural dynamic response and the aerodynamics of the wind turbine can be considered in a quasi-steady manner by means of the aerodynamic damping. The aerodynamic damping estimates obtained from the method proposed by Valamanesh and Myers [32] were compared with those identified from the recorded accelerations of the wind turbine model in the experiments under different operational cases. The results demonstrate that this method yields good estimates of the aerodynamic damping, which gives a necessary experimental support to the method. This is significant because a reliable aerodynamic damping model is necessary to analyze the loads accurately during the design stage.
2) Compared to the earthquake-only scenario, the interaction between the wind and the seismic-induced loads could lead to a reduction of the overall response. To take this interaction into account without conducting time-consuming fully-coupled aeroelastic analysis, the individual wind and seismic responses can be treated separately by including an appropriate aerodynamic damping in the latter and by combining the two isolated responses in an adequate way. Three different rules of combination were investigated. The $\eta = 1$ combination (i.e. the simple sum of the two separate responses) tends to render over-conservative results, whereas the $\eta = 0.75$ combination underestimates the responses. The SRSS combination is recommended in this research in light of the better prediction of the fully-coupled wind-seismic responses obtained experimentally.
3) The FAST simulation was performed to explore the influence of different ratios of the wind/earthquake induced responses on the assessment of the dynamic behavior of wind turbine structures by means of the simplified method that considers both actions separately. The numerical simulation in FAST was in good agreement with the experimental results. The coupling effect between the wind and the earthquake responses tends to increase with the wind speed and to decrease with the PGA. For moderate wind/seismic response ratios (in the order of 0.05 – 0.3), the SRSS combination method is again recommended because it gives estimates of the fully-coupled wind-seismic response that are reasonably on the safe side. In addition, it is found that the higher vibration modes of the tower have a negligible contribution to the tower responses, and therefore the turbine model in this work can be considered as a two-directional SDOF system for the aerodynamic damping calculation. The numerical simulation in FAST also indicates that the aerodynamic interaction between wind and earthquake actions only occurs in the fore-aft direction, parallel to the incoming wind.

The carefully designed model and validated incoming wind flow ensure the effectiveness of the experimental results to support the estimation of the aerodynamic damping of wind turbines subject to ground motions. The results of this work contribute to the understanding of the interaction between wind and earthquake actions in wind turbines in operation, and it provides engineers with an experimental reference to include appropriate aerodynamic damping in the analysis, as well as suitable load combination methods to obtain the design demand using simplified calculations. In addition, this work describes the blade design and other aspects of the physical model of a wind turbine for small-scale testing, observing a good agreement between the experimental and the numerical results. This contributes a helpful experience for the design of larger-scale experiments in the future. However, the conclusions in this work are based on the study of a simplified wind turbine model in which the influence of the electro-mechanical control system (e.g.

torque-pitch control for the regulation of the output power) is not considered. Future experimental works on models with the inclusion of the control system could further explore the complex interaction effects among the earthquake, the wind and the control-induced motions.

Acknowledgements

The authors would like to acknowledge the support from National Natural Science Foundation of China [grant number 51878426]; International Collaboration Program of Science and Technology Commission of Ministry of Science and Technology, China [grant number 2016YFE0105600]; International Collaboration Program of Science and Technology Commission of Shanghai Municipality and Sichuan Province [grant numbers 16510711300, 18GJHZ0111]; and the Fundamental Research Funds for Central Universities of China.

Declaration of interest

None.

References

[1] GWEC. (2019). Global Wind Report 2018. Brussels, Belgium: Global Wind Energy Council.

[2] IRENA. (2019). Renewable Power Generation Costs in 2018. Abu Dhabi, United Arab Emirates: International Renewable Energy Agency.

[3] Burton, T., Jenkins, N., Sharpe, D., & Bossanyi, E. (2011). Wind Energy Handbook. Chichester, UK: John Wiley & Sons, Ltd. https://doi.org/10.1002/9781119992714.

[4] Hansen, M. O. (2015). Aerodynamics of Wind Turbines. London: Routledge. http://dx.doi.org/10.4324/9781315769981.

[5] De Risi, R., Bhattacharya, S., & Goda, K. (2018). Seismic performance assessment of monopile-supported offshore wind turbines using unscaled natural earthquake records. Soil Dynamics and Earthquake Engineering, 109(March), 154–172. https://doi.org/10.1016/j.soildyn.2018.03.015.

[6] Katsanos, E. I., Thöns, S., & Georgakis, C. T. (2016). Wind turbines and seismic hazard: a state-of-the-art review. Wind Energy, 19(11), 2113-2133. https://doi.org/10.1002/we.1968.

[7] Smith, V., & Mahmoud, H. (2016). Multihazard Assessment of Wind Turbine Towers under Simultaneous Application of Wind, Operation, and Seismic Loads. Journal of Performance of Constructed Facilities, 30(6), 04016043. https://doi.org/10.1061/(ASCE)CF.1943-5509.0000898.

[8] Dai, K., Huang, Y., Gong, C., Huang, Z., & Ren, X. (2015). Rapid seismic analysis methodology for in-service wind turbine towers. Earthquake Engineering and Engineering Vibration, 14(3), 539-548. https://doi.org/10.1007/s11803-015-0043-0.

[9] Patil, A., Jung, S., & Kwon, O. S. (2016). Structural performance of a parked wind turbine tower subjected to strong ground motions. Engineering Structures, 120, 92–102. https://doi.org/10.1016/j.engstruct.2016.04.020.

[10] Sadowski, A. J., Camara, A., Málaga-Chuquitaype, C., & Dai, K. (2017). Seismic analysis of a tall metal wind turbine support tower with realistic geometric imperfections. Earthquake Engineering & Structural Dynamics, 46(2), 201-219. https://doi.org/10.1002/eqe.2785.

[11] Zhao, Z., Dai, K., Camara, A., Bitsuamlak, G., & Sheng, C. (2019). Wind Turbine Tower Failure Modes under Seismic and Wind Loads. Journal of Performance of Constructed Facilities, 33(2), 04019015. https://doi.org/10.1061/(ASCE)CF.1943-5509.0001279.

[12] Asareh, M., Schonberg, W., & Volz, J. (2016). Fragility analysis of a 5-MW NREL wind turbine considering aero-elastic and seismic interaction using finite element method. Finite Elements in Analysis and Design, 120, 57-67. https://doi.org/10.1016/j.finel.2016.06.006.

[13] ASCE/AWEA. (2011). Recommended practice for compliance of large onshore wind turbine support structures (ASCE/AWEA RP2011). Washington DC: American Wind Energy Association.

[14] Prowell, I. (2011). An experimental and numerical study of wind turbine seismic behavior. Ph.D. Dissertation, University of

602 California, San Diego.
603 [15] Asareh, M. (2015). Dynamic behavior of operational wind turbines considering aerodynamic and seismic load interaction. Ph.D.
604 Dissertation, Missouri University of Science and Technology.
605 [16] Asareh, M., Schonberg, W., & Volz, J. (2016). Effects of seismic and aerodynamic load interaction on structural dynamic
606 response of multi-megawatt utility scale horizontal axis wind turbines. Renewable Energy, 86, 49–58.
607 https://doi.org/10.1016/j.renene.2015.07.098.
608 [17] Yuan, C., Chen, J., Li, J., & Xu, Q. (2017). Fragility analysis of large-scale wind turbines under the combination of seismic and
609 aerodynamic loads. Renewable Energy, 113, 1122-1134. https://doi.org/10.1016/j.renene.2017.06.068.
610 [18] Santangelo, F., Failla, G., Santini, A., & Arena, F. (2016). Time-domain uncoupled analyses for seismic assessment of land-
611 based wind turbines. Engineering Structures, 123, 275–299. https://doi.org/10.1016/j.engstruct.2016.05.043.
612 [19] Jonkman, J. M., & Buhl Jr, M. L. (2005). FAST user's guide. Golden: National Renewable Energy Laboratory. Technical Report
613 No. NREL/EL-500-38230.
614 [20] Bossanyi, E. A. (2003). GH bladed theory manual. Garrad Hassan & Partners Ltd, 2, 56-58.
615 [21] Santangelo, F., Failla, G., Arena, F., & Ruzzo, C. (2018). On time-domain uncoupled analyses for offshore wind turbines under
616 seismic loads. Bulletin of Earthquake Engineering, 16(2), 1007–1040. https://doi.org/10.1007/s10518-017-0191-x.
617 [22] IEC. (2005). IEC 61400-1 Ed. 3: Wind Turbines - Part 1: Design Requirements. Geneva, Switzerland: International
618 Electrotechnical Commission.
619 [23] GL. (2010). Guideline for the certification of wind turbines. Hamburg, Germany: Germanischer Lloyd.
620 [24] Avossa, A. M., Demartino, C., Contestabile, P., Ricciardelli, F., & Vicinanza, D. (2017). Some results on the vulnerability
621 assessment of HAWTs subjected to wind and seismic actions. Sustainability (Switzerland), 9(9), 1–16.
622 https://doi.org/10.3390/su9091525.
623 [25] Liu, X., Lu, C., Li, G., Godbole, A., & Chen, Y. (2017). Effects of aerodynamic damping on the tower load of offshore horizontal
624 axis wind turbines. Applied Energy, 204, 1101–1114. https://doi.org/10.1016/j.apenergy.2017.05.024.
625 [26] Zhang, R., Zhao, Z., & Dai, K. (2019). Seismic response mitigation of a wind turbine tower using a tuned parallel inerter mass
626 system. Engineering Structures, 180, 29-39. https://doi.org/10.1016/j.engstruct.2018.11.020.
627 [27] Dai, K., Wang, Y., Huang, Y., Zhu, W., & Xu, Y. (2017). Development of a modified stochastic subspace identification method
628 for rapid structural assessment of in-service utility-scale wind turbine towers. Wind Energy, 20(10), 1687- https://doi.org/1710.
629 10.1002/we.2117.
630 [28] Dong, X., Lian, J., Wang, H., Yu, T., & Zhao, Y. (2018). Structural vibration monitoring and operational modal analysis of
631 offshore wind turbine structure. Ocean Engineering, 150(92), 280–297. https://doi.org/10.1016/j.oceaneng.2017.12.052.
632 [29] Carswell, W., Johansson, J., Løvholt, F., Arwade, S. R., Madshus, C., DeGroot, D. J., & Myers, A. T. (2015). Foundation
633 damping and the dynamics of offshore wind turbine monopiles. Renewable Energy, 80, 724–736.
634 https://doi.org/10.1016/j.renene.2015.02.058.
635 [30] Witcher, D. (2005). Seismic analysis of wind turbines in the time domain. Wind Energy, 8(1), 81–91.
636 https://doi.org/10.1002/we.135.
637 [31] ASCE. (2010). Minimum design loads for buildings and other structures (ASCE/SEI 7-10). Reston, VA: American Society of
638 Civil Engineers.
639 [32] Valamanesh, V., & Myers, A. T. (2014). Aerodynamic Damping and Seismic Response of Horizontal Axis Wind Turbine
640 Towers. Journal of Structural Engineering, 140(11), 04014090. https://doi.org/10.1061/(ASCE)ST.1943-541X.0001018.
641 [33] Prowell, I., Elgamal, A., Uang, C.-M., Enrique Luco, J., Romanowitz, H., & Duggan, E. (2014). Shake table testing and
642 numerical simulation of a utility-scale wind turbine including operational effects. Wind Energy, 17(7), 997–1016.
643 https://doi.org/10.1002/we.1615.
644 [34] Garrad, A. D. (1990). Forces and dynamics of horizontal axis wind turbines. Wind energy conversion systems, 119-144.
645 [35] Kühn, M. J. (2001). Dynamics and design optimisation of offshore wind energy conversion systems. DUWIND, Delft University
646 Wind Energy Research Institute. Report2001.002.

[36] Salzmann, D. C., & Van der Tempel, J. (2005). Aerodynamic damping in the design of support structures for offshore wind turbines. Proceedings of the Offshore Wind Energy Conference. Copenhagen, Denmark.

[37] Yang, Y., Ye, K., Li, C., Michailides, C., & Zhang, W. (2018). Dynamic behavior of wind turbines influenced by aerodynamic damping and earthquake intensity. Wind Energy, 21(5), 303–319. https://doi.org/10.1002/we.2163.

[38] McTavish, S., Feszty, D., & Nitzsche, F. (2013). Evaluating Reynolds number effects in small-scale wind turbine experiments. Journal of Wind Engineering and Industrial Aerodynamics, 120, 81–90. https://doi.org/10.1016/j.jweia.2013.07.006.

[39] Campagnolo, F. (2013). Wind tunnel testing of scaled wind turbine models: aerodynamics and beyond. Ph.D. Dissertation, Politecnico di Milano.

[40] Martin, H. R., Kimball, R. W., Viselli, A. M., & Goupee, A. J. (2014). Methodology for wind/wave basin testing of floating offshore wind turbines. Journal of Offshore Mechanics and Arctic Engineering, 136(2), 020905. https://doi.org/10.1115/1.4025030.

[41] McGhee, R., Walker B., & Millard B. (1988). Experimental results for the Eppler 387 airfoil at low Reynolds numbers in the Langley Low-Turbulence Pressure Tunnel. NASA TM 4062, NASA.

[42] Selig, M., Guglielmo, J., Broeren, A., & Giguère, P. (1995). Summary of Low-Speed Airfoil Data, vol. 1. SoarTech Publications, Virginia Beach, VA.

[43] Sahin, M., Hall, J., Mohseni, K., & Hillewaert, K. (2008). Direct Numerical Simulation of Separated Low-Reynolds Number Flows around an Eppler 387 Airfoil. 46th AIAA Aerospace Sciences Meeting and Exhibit, 1–28. https://doi.org/10.2514/6.2008-422.

[44] McArthur, J. (2008). Aerodynamics of wings at low Reynolds numbers: Boundary layerseparation and reattachment. Ph.D. Dissertation, University of Southern California.

[45] Hassanzadeh, A., Naughton, J. W., Kelley, C. L., & Maniaci, D. C. (2016). Wind turbine blade design for subscale testing. In: IOP publishing Journal of Physics Conference Series, Vol. 753, No. 2, p. 022048. https://doi.org/10.1088/1742-6596/753/2/022048.

[46] Ryi, J., Rhee, W., Hwang, U. C., & Choi, J. S. (2015). Blockage effect correction for a scaled wind turbine rotor by using wind tunnel test data. Renewable Energy, 79, 227-235. https://doi.org/10.1016/j.renene.2014.11.057.

[47] Bottasso, C. L., Campagnolo, F., & Petrović, V. (2014). Wind tunnel testing of scaled wind turbine models: Beyond aerodynamics. Journal of Wind Engineering and Industrial Aerodynamics, 127, 11-28. https://doi.org/10.1016/j.jweia.2014.01.009.

[48] Li, L., Gao, Y., Hu, Z., Yuan, Z., Day, S., & Li, H. (2018). Model test research of a semisubmersible floating wind turbine with an improved deficient thrust force correction approach. Renewable Energy, 119, 95-105. https://doi.org/10.1016/j.renene.2017.12.019.

[49] Duan, F., Hu, Z., Liu, G., & Wang, J. (2016). Experimental comparisons of dynamic properties of floating wind turbine systems based on two different rotor concepts. Applied Ocean Research, 58, 266-280. https://doi.org/10.1016/j.apor.2016.04.012.

[50] Berger, F., Kröger, L., Onnen, D., Petrović, V., & Kühn, M. (2018). Scaled wind turbine setup in a turbulent wind tunnel. In: IOP publishing Journal of Physics Conference Series, Vol. 1104, No. 1, p. 012026. https://doi.org/10.1088/1742-6596/1104/1/012026.

[51] Bayati, I., Belloli, M., Bernini, L., & Zasso, A. (2017). Aerodynamic design methodology for wind tunnel tests of wind turbine rotors. Journal of Wind Engineering and Industrial Aerodynamics, 167, 217-227. https://doi.org/10.1016/j.jweia.2017.05.004.

[52] Nanos, E. M., Kheirallah, N., Campagnolo, F., & Bottasso, C. L. (2018). Design of a multipurpose scaled wind turbine model. In: IOP publishing Journal of Physics Conference Series, Vol. 1037, No. 5, p. 052016. https://doi.org/10.1088/1742-6596/1037/5/052016.

[53] Coudou, N., Buckingham, S., Bricteux, L., & van Beeck, J. (2018). Experimental Study on the Wake Meandering Within a Scale Model Wind Farm Subject to a Wind-Tunnel Flow Simulating an Atmospheric Boundary Layer. Boundary-layer meteorology, 167(1), 77-98. https://doi.org/10.1007/s10546-017-0320-8.

[54] Lanzafame, R., & Messina, M. (2010). Power curve control in micro wind turbine design. Energy, 35(2), 556–561.

https://doi.org/10.1016/j.energy.2009.10.025.
[55] Akour, S. N., Al-Heymari, M., Ahmed, T., & Khalil, K. A. (2018). Experimental and theoretical investigation of micro wind turbine for low wind speed regions. Renewable Energy, 116, 215–223. https://doi.org/10.1016/j.renene.2017.09.076.
[56] Quanser Inc. (2014). Shake Table II User Manual. Ontario, Canada: Quanser Inc.
[57] Yalla, S. K., & Kareem, A. (2001). Beat phenomenon in combined structure-liquid damper systems. Engineering Structures, 23(6), 622-630. https://doi.org/10.1016/S0141-0296(00)00085-7.
[58] Castellani, F., Astolfi, D., Becchetti, M., Berno, F., Cianetti, F., & Cetrini, A. (2018). Experimental and numerical vibrational analysis of a horizontal-axis micro-wind turbine. Energies, 11(2). https://doi.org/10.3390/en11020456.
[59] Koukoura, C., Natarajan, A., & Vesth, A. (2015). Identification of support structure damping of a full scale offshore wind turbine in normal operation. Renewable energy, 81, 882-895. https://doi.org/10.1016/j.renene.2015.03.079.
[60] Wang, S., Zhou, Y., Alam, M. M., & Yang, H. (2014). Turbulent intensity and Reynolds number effects on an airfoil at low Reynolds numbers. Physics of Fluids, 26(11), 115107. https://doi.org/10.1063/1.4901969.
[61] Istvan, M. S., & Yarusevych, S. (2018). Effects of free-stream turbulence intensity on transition in a laminar separation bubble formed over an airfoil. Experiments in Fluids, 59(3), 52. https://doi.org/10.1007/s00348-018-2511-6.
[62] CMC. (2010). Code for Seismic Design of Buildings (GB50011-2010). Beijing, China: China Ministry of Construction, China Architecture and Building Press. (in Chinese)
[63] Ancheta, T. D., Darragh, R. B., Stewart, J. P., Seyhan, E., Silva, W. J., Chiou, B. S. J., ... & Kishida, T. (2014). NGA-West2 database. Earthquake Spectra, 30(3), 989-1005. https://doi.org/10.1193/070913EQS197M.

Appendix

Table A.1 Application of two different methods for the estimation of the aerodynamic damping

Wind speed (V_W)			7 m/s		Indoor temperature (T)				22.0 °C		
Rotor speed (N)			855 rpm		Density of air (ρ)				1.205 kg/m^3		
Pitch angle			0		Kinematic viscosity of air (υ)				1.8×10^{-5} kg/(m·s)		
r	c	β	a	a'	φ	α	Re	C_L	C_L'	C_D	C_D'
[mm]	[mm]	[deg]	[-]	[-]	[deg]	[deg]	[-]	[-]	[-]	[-]	[-]
80	78.025	18.146	0.229	0.081	34.888	16.742	40926	0.8537	-0.0269	0.2273	-0.0300
96	72.497	15.258	0.314	0.097	27.001	11.743	42620	1.1074	0.0875	0.1204	0.0350
112	66.947	12.748	0.307	0.070	24.332	11.584	43812	1.0920	0.1063	0.1175	0.0367
128	61.649	10.588	0.302	0.053	22.051	11.463	44581	1.0782	0.1201	0.1153	0.0380
144	56.767	8.749	0.299	0.041	20.094	11.345	45051	1.0633	0.1329	0.1132	0.0392
160	52.355	7.168	0.298	0.032	18.384	11.216	45307	1.0453	0.1460	0.1109	0.0405
176	48.354	5.770	0.301	0.026	16.841	11.071	45357	1.0231	0.1593	0.1084	0.0419
192	44.596	4.481	0.310	0.021	15.386	10.905	45092	0.9955	0.1725	0.1055	0.0435
208	40.804	3.191	0.331	0.017	13.897	10.706	44232	0.9600	0.1850	0.1021	0.0454
224	36.586	1.799	0.374	0.014	12.160	10.361	42273	0.8938	0.1970	0.0965	0.0486
240	31.442	0.172	0.689	0.007	5.753	5.581	37975	0.6010	0.0289	0.0405	0.0748
Method of Valamanesh and Myers [32]			$c_{fore-aft} = 0.1373$; $c_{side-side} = 0.0109$				Method of Kühn [35]		$c_{fore-aft} = 0.0287$		

Table A.2. Error propagation for the measurement and calculation of aerodynamic damping in the fore-aft direction

Error propagation **Case:** wind speed = 7 m/s, rotor speed = 855 rpm, pitch angle = 0º		
Aerodynamic damping measured experimentally	Total damping $\omega\zeta_{tot}$ [rad/s]	5 measurements: [0.7588, 0.7457, 0.7546, 0.7695, 0.7541]

		$\mu_{(\omega\zeta)_{tot}} = 0.7565,\ \sigma_{(\omega\zeta)_{tot}} = 0.00775,\ \delta_{(\omega\zeta)_{tot}} = 0.0035$
	Structural damping $\omega\zeta_{st}$ [rad/s]	7 measurements: [0.7096, 0.6971, 0.7040, 0.7043, 0.7031, 0.7085, 0.7048] $\mu_{(\omega\zeta)_{st}} = 0.7045,\ \sigma_{(\omega\zeta)_{st}} = 0.00376,\ \delta_{(\omega\zeta)_{tot}} = 0.0014$
	Aerodynamic damping c_{aero} [kg/s]	$\mu_{c_{aero}} = 2m\left[\mu_{(\omega\zeta)_{tot}} - \mu_{(\omega\zeta)_{st}}\right] = 0.1275\ \ \delta_{c_{aero}} = 2m\sqrt{\delta^2_{(\omega\zeta)_{tot}} + \delta^2_{(\omega\zeta)_{st}}} = 0.0092$
	Final result	$c_{aero} = 0.127 \pm 0.009\ kg/s$
Wind speed V_W [m/s]		$\mu_{V_W} = 7.012,\ \sigma_{V_W} = 0.355,\ \ \delta_{V_W} = 0.014$
Rotational frequency Ω [rad/s]		$\mu_\Omega = 89.5,\ \sigma_\Omega = 9.8,\ \delta_\Omega = 1.0$
Aerodynamic damping calculated from method 1	Aerodynamic damping c_{aero} [kg/s]	$\mu_{c_{aero}} = k_1\mu_{V_W} + k_2\mu_\Omega = 0.1375$ $\delta_{c_{aero}} = \sqrt{k_1^2\delta^2_{V_W} + k_2^2\delta^2_\Omega} = 0.0004$
	Final result	$c_{aero} = 0.1375 \pm 0.0004\ kg/s$
Aerodynamic damping calculated from method 2	Aerodynamic damping c_{aero} [kg/s]	$\mu_{c_{aero}} = k\mu_\Omega = 0.0287\ ,\ \ \delta_{c_{aero}} = k\delta_\Omega = 0.0003$
	Final result	$c_{aero} = 0.0287 \pm 0.0003\ kg/s$
Nomenclature	μ: Mean σ: Standard Deviation δ: Standard Error (error in the mean) k, k_1, k_2: Sensitivity coefficient (related to formula to calculate aerodynamic damping)	

714

Nomenclature

a	axial induction factor [-]	N	rotor speed [rpm]
a'	tangential induction factor [-]	N_b	number of blades [-]
b	aerodynamic damping correction factor [-]	Re	Reynolds number [-]
c	blade chord length [mm]	r	local radial distance of the blade section with respect to the blade root [mm]
$c_{fore\text{-}aft}$	aerodynamic damping coefficient in the fore-aft direction [N·s/m]	T	thrust force [N]
$c_{side\text{-}side}$	aerodynamic damping coefficient in the side-side direction [N·s/m]	T_u	free-stream turbulence intensity [%]
C_D	sectional drag coefficient [-], $C_D = D/(0.5\rho c V_{rel}^2)$	V_W	wind velocity in the fore-aft direction [m/s]
C_D'	derivative of drag coefficient with respect to angle of attack [-], $C_D' = \mathrm{d}C_D/\mathrm{d}\alpha$	V_{rel}	relative wind velocity [m/s]
C_L	sectional lift coefficient [-], $C_L = L/(0.5\rho c V_{rel}^2)$	*Greek letters*	
C_L'	derivative of lift coefficient with respect to angle of attack [-], $C_L' = \mathrm{d}C_L/\mathrm{d}\alpha$	α	angle of attack [deg], the angle between V_{rel} and the chord line
C_P	sectional power coefficient [-], $C_P = P/(0.5\rho c V_{rel}^3)$	β	twist angle [deg], the angle between the rotor plane and the chord line
D	drag force [N]	φ	inflow angle [deg], the angle between the rotor plane and V_{rel}
F	overall Prandtl's loss factor [-], $F = F_{tip} \cdot F_{root}$	λ	local speed ratio [-], $\lambda = \Omega r/V_W$
F_{tip}	Prandtl's tip loss factor [-]	λ_T	tip speed ratio (TSR) [-], $\lambda_T = \Omega R/V_W$
F_{root}	Prandtl's root loss factor [-]	ω	angular frequency [rad/s], $\omega = 2\pi f_n$

L	lift force [N]	Ω	rotational frequency [rad/s], $\Omega = 2\pi N/60$

715